iScience

CellPress
OPEN ACCESS

Article

Uncovering specificity of endogenous TAU aggregation in a human iPSC-neuron TAU seeding model

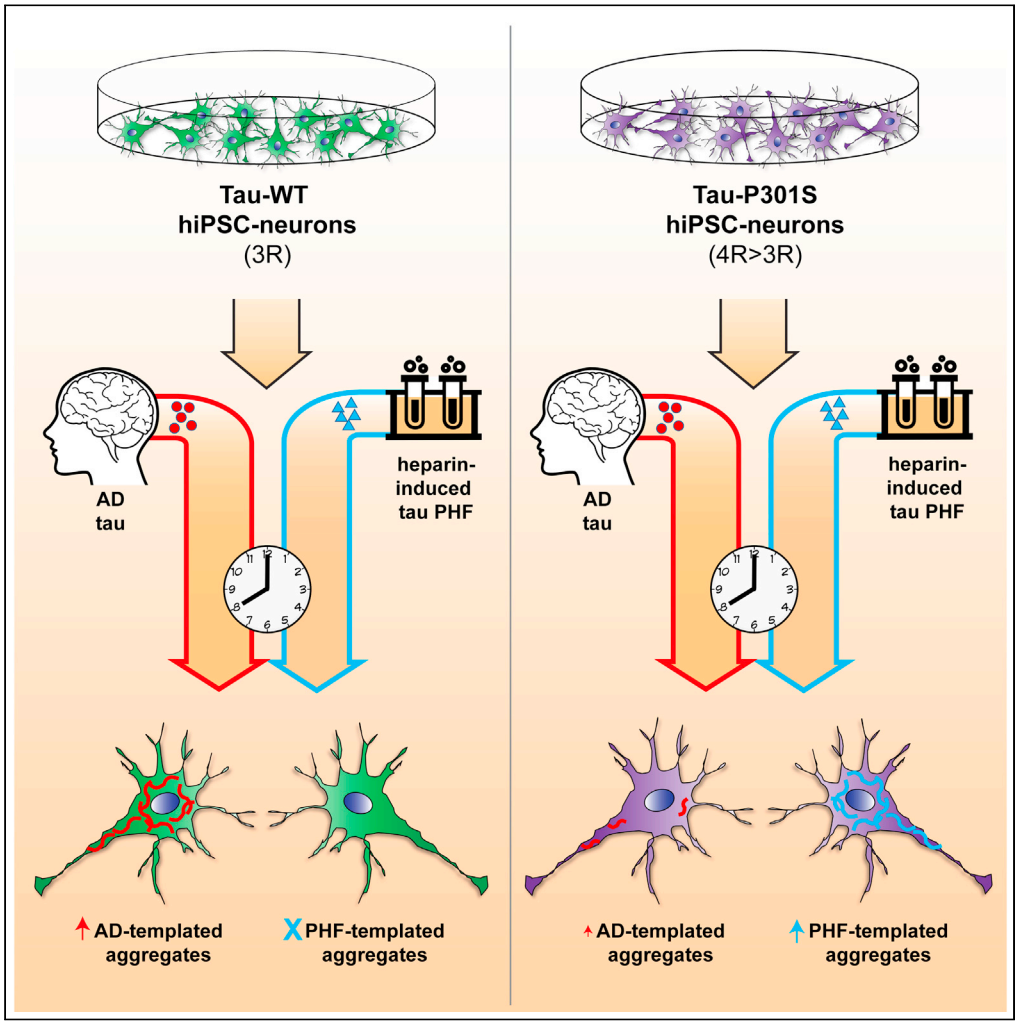

Justine D. Manos, Christina N. Preiss, Nandini Venkat, ..., Katherine Titterton, Eric Karran, Xavier Langlois

justine.manos@abbvie.com

Highlights

Seeded tau aggregation in hiPSC-neurons does not require tau overexpression

Tau aggregation is concentration, time, and maturation dependent

Successful templating requires compatibility between neuronal tau and added seeds

Endogenous tau aggregates exhibit properties consistent with pathological tau

Manos et al., iScience 25, 103658
January 21, 2022
https://doi.org/10.1016/j.isci.2021.103658

iScience

CellPress
OPEN ACCESS

Article

Uncovering specificity of endogenous TAU aggregation in a human iPSC-neuron TAU seeding model

Justine D. Manos,[1,4,*] Christina N. Preiss,[1] Nandini Venkat,[1] Joseph Tamm,[1] Peter Reinhardt,[2] Taekyung Kwon,[1] Jessica Wu,[1] Allison D. Winter,[3] Thomas R. Jahn,[2] Kiran Yanamandra,[1] Katherine Titterton,[1] Eric Karran,[1] and Xavier Langlois[1]

SUMMARY

Tau pathobiology has emerged as a key component underlying Alzheimer's disease (AD) progression; however, human neuronal *in vitro* models have struggled to recapitulate tau phenomena observed *in vivo*. Here, we aimed to define the minimal requirements to achieve endogenous tau aggregation in functional neurons utilizing human induced pluripotent stem cell (hiPSC) technology. Optimized hiPSC-derived cortical neurons seeded with AD brain-derived competent tau species or recombinant tau fibrils displayed increases in insoluble, endogenous tau aggregates. Importantly, *MAPT*-wild type and *MAPT*-mutant hiPSC-neurons exhibited unique propensities for aggregation dependent on the seed strain rather than the repeat domain identity, suggesting that successful templating of the recipient tau may be driven by the unique conformation of the seed. The *in vitro* model presented here represents the first successful demonstration of combining human neurons, endogenous tau expression, and AD brain-derived competent tau species, offering a more physiologically relevant platform to study tau pathobiology.

INTRODUCTION

Tau is a naturally unfolded and highly soluble protein that stabilizes microtubules in axons. It undergoes a series of post-translational modifications, mislocalization, and conformational changes in neurodegenerative diseases collectively known as tauopathies (Mandelkow and Mandelkow, 1998). In Alzheimer's disease (AD), the intraneuronal accumulation of hyperphosphorylated tau into aggregates known as neurofibrillary tangles (NFTs) has been shown to be correlated with the cognitive decline observed in patients with AD (Arriagada et al., 1992; Braak and Braak, 1991), suggesting that interdicting tau aggregation could slow down disease progression (Brunden et al., 2009).

Human induced pluripotent stem cell (hiPSC) technology offers many opportunities to uncover species-specific mechanisms of tau aggregation and transmission *in vitro*. Reprogramming and differentiation have enabled the study of both familial and sporadic AD in neurons originating from patient cells, demonstrating early events including increases in Aβ42 production and tau hyperphosphorylation (Mungenast et al., 2016; Tcw, 2019). Yet recapitulating tau aggregation in AD patient-specific hiPSC-derived neurons has remained elusive (Allsopp et al., 2019). These results likely reflect the difficulty of modeling diseases with adult or late onset in immature hiPSC-neurons (Brennand et al, 2015) that would require many years to spontaneously present disease-associated phenotypes.

One strategy to circumvent these technical limitations is to develop a model in which self-assembly of endogenous tau is caused by the addition of an exogenous "seed" template as has been successfully demonstrated in mouse primary neurons (Guo and Lee, 2011; Dujardin et al, 2020). However, hiPSC-neuron tau seeding models have not matched the success of mouse primary neurons for studying tau pathobiology, motivating the continued search for a more physiologically relevant model (Chang et al, 2021). Reports of hiPSC-neuron models to date reveal inconsistencies with regards to the formation of insoluble tau aggregates and often show a requirement for tau overexpression or tau seed concentrations in excess of

[1]Abbvie, Cambridge Research Center, 200 Sidney Street, Cambridge, MA 02139, USA

[2]AbbVie Deutschland GmbH & Co. KG, Neuroscience Research, Knollstrasse, 67061 Ludwigshafen, Germany

[3]Northeastern University, 360 Huntington Avenue, Boston, MA 02115, USA

[4]Lead contact

*Correspondence: justine.manos@abbvie.com

https://doi.org/10.1016/j.isci.2021.103658

50 nM similar to HEK cells (García-León et al., 2018; Medda et al, 2016; Usenovic et al, 2015; Verheyen et al, 2015, 2018). Here we aimed to address these challenges by optimizing a standardized protocol for differentiation with quality control measures that enable reproducible generation and distribution of cortical neurons from hiPSCs. Utilizing isogenic hiPSC lines, we explored the minimal requirements needed to achieve *in vitro* endogenous tau aggregation by assessing the contribution of mutations that favor tau with 4-repeat domains (4R tau) and pro-aggregation mutations without overexpression. A variety of sources of exogenously added tau seeds were tested at minimal concentrations, showing that aggregation in this hiPSC-neuron paradigm is dependent on (1) the presence of tau, (2) the seed concentration, (3) the time of addition of seeds, (4) the recipient tau species, and (5) the seed strain. Combining compatible hiPSC-neurons and tau seeds resulted in robust tau aggregation that could be labeled by a variety of anti-pathological tau antibodies (APTAs).

RESULTS

Differentiation to disease-relevant neurons

Establishing an *in vitro* neuronal model of AD-relevant tau aggregation requires differentiating hiPSCs to neurons expressing markers consistent with a brain region that is affected in the disease (Mungenast et al., 2016). Given the reported vulnerability of cortical excitatory neurons in AD (Fu et al, 2018; Verheyen et al, 2018), we first set out to optimize the conversion of hiPSCs to homogeneous cortical excitatory neurons and define quality control assessments at intermediate stages to ensure confidence and consistency across independent batches. Using a small molecule cocktail previously described (Cao et al, 2017; Chambers et al, 2009; Gaspard et al, 2008), hiPSCs transitioned over a 25-day period from neuroepithelial progenitors to a lawn of neural rosettes that do not require manual isolation, and then finally to a mixed culture of neural progenitors and cortical neurons that can be re-plated at low density to achieve a distributed neuronal network that matures over time (Figure 1A). At day 10 of the differentiation, we evaluated expression of Pax6 (neuroectoderm) as well as markers associated with common contaminants, including Sox10 (neural crest) and AP2α (non-neural ectoderm), using a cutoff of >80% PAX6, <1% Sox10, <1% AP2α to define a successful batch (Figure 1B). Synchronization of the final conversion of neural progenitors to terminally differentiated neurons was achieved via short-term treatment with the γ-secretase inhibitor RO4929097 to inhibit Notch signaling (Borghese et al, 2010) (Figure 1C). Similar to DAPT, RO4929097 reduced the expression of genes associated with neural progenitors (e.g., *SOX1*) and increased the expression of genes associated with neuron maturation (e.g., *SYP;* Figure S1A). Important for developing an AD-relevant model, short-term treatment did not show prolonged interference of APP processing (Figure S1B). To further eliminate the remaining proliferative neural progenitor cells, treatment with mitomycin C, a DNA alkylating and cross-linking reagent that does not affect post-mitotic neurons (Hiller et al, 2020), was found to increase the homogeneity of the neuron cultures (Figure S1C). Finally, to facilitate high-throughput applications, the plate manufacturer, coating, and cell density were optimized in a 96-well plate format to achieve a uniform layer of hiPSC-neurons that would enable quantitative high content imaging (Figure 1D). The optimized protocol resulted in hiPSC-neurons expressing pan-neuronal (MAP2, TUBB3, tau), telencephalic (FOXG1), and cortical layer (TBR1, CTIP2) markers consistent with a deep layer cortical neuron identity (Figure 1E). The progression of the hiPSCs through the developmental stages was also confirmed using a quantitative PCR panel of 96 genes, demonstrating consistent specification of excitatory cortical neurons through a telencephalic neural progenitor across independent donor lines (Figures 1F and S1D). Functional evaluation of these hiPSC-neurons by calcium imaging showed an increase in cofiring activity as the neurons matured (Figure S1E), and healthy cultures could be maintained for at least 6 months (Figure S1F).

Formation of insoluble tau aggregates does not require tau overexpression

Previous studies (Lim et al, 2014; Medda et al, 2016; Verheyen et al, 2015) have suggested that tau aggregation in hiPSC-neurons in response to exogenous seeds requires overexpression of tau bearing P301 mutations, which enhance its propensity to form beta-pleated sheets (Mocanu et al, 2008; Santacruz et al, 2005). However, these studies also utilized recombinant tau seeds that do not recapitulate the structural properties found in AD brain-derived tau (Zhang et al, 2019). In order to work toward an improved translational human model of tau aggregation, we first evaluated whether endogenous aggregation could be induced in response to AD brain-derived tau species in *MAPT-WT* hiPSC-neurons. Using our optimized differentiation platform, *MAPT*-WT hiPSC-neurons exhibited pan-neuronal markers and markers of a deep layer excitatory identity (Figures S2A–S2D). After maturation for 16 days *in vitro* (DIV 16) on the final assay plate (Figure 2A), *MAPT*-WT hiPSC-neurons were treated with up to 1 nM tau protein immunopurified from AD brain lysate using MC1, an anti-tau antibody directed against a pathological conformation (Jicha et al.,

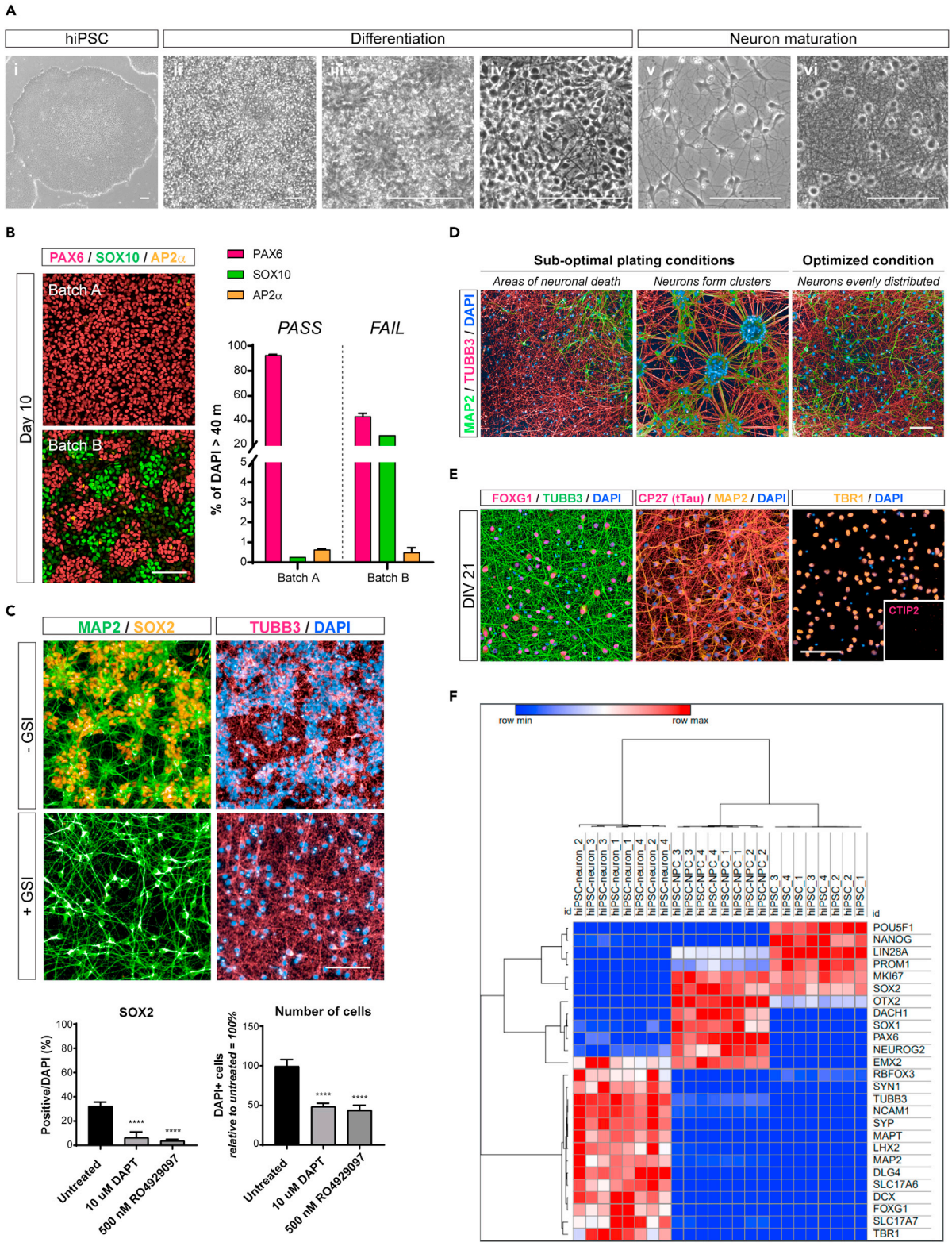

Figure 1. Standardization of a robust platform for hiPSC conversion to cortical neurons

(A) Representative phase-contrast images showing the expected morphology of hiPSCs throughout differentiation into hiPSC-neurons. i: hiPSC before harvesting; ii: day 9; iii: day 15; iv: day 25; v: day 28/DIV 3; vi: day 46/DIV 21. DIV indicates day *in vitro* of neuronal maturation.

Figure 1. *Continued*

(B) Day 10 checkpoint comparing the immunofluorescence (IF) staining (*left*) and quantification (*right*) of "pass" (PAX6 >80%; SOX10 < 1%, AP2α <1%) and "fail" batches. Graph represents mean +SD (n = 3 replicate wells, 25 fields per well).

(C) Representative IF images and quantification reveal a reduction in SOX2+ proliferative neural progenitor cells and total cell number following treatment with the γ-secretase inhibitors (GSI) DAPT or RO4929097, resulting in a more homogeneous neuronal (MAP2/TUBB3+) population. Graphs represent mean +SD (n = 3 replicate wells, 30 fields per well). ****p < 0.0001 according to one-way ANOVA with Dunnett's test.

(D) Plating conditions were optimized to reduce cell toxicity, prevent clumping, and achieve an evenly distributed MAP2+/TUBB3+ neurite network. Optimal conditions are described in the STAR methods section.

(E) DIV21 hiPSC-neurons express pan-neuronal markers including TUBB3, MAP2, and CP27 (human total tau) as well as markers consistent with a telencephalic (FOXG1), deep layer (TBR1) cortical identity.

(F) Heatmap with unbiased hierarchical clustering depicts a subset of differentially expressed genes at the hiPSC, hiPSC-NPC, and hiPSC-neuron stages, demonstrating consistency and reproducibility in producing a cortical excitatory fate. Relative expression values are scaled per gene to indicate the cell stage with the highest expression. Scale bars: 100 μm. See also Figure S1.

1997). MC1-purified AD brain material (MC1-AD) exhibited hyperphosphorylated tau species denoted by the higher-molecular-weight species compared with control and by recognition with PHF1 similar to crude AD lysate (Figure S2E). When applied to hiPSC-neurons, MC1-AD seeds showed a time-dependent increase in association with neurites from 1 to 24 h (Figures 2B and 2C). Seven weeks post seeding, the neurons were fixed with methanol to remove soluble tau species (Guo et al., 2016) and stained with MC1 to visualize insoluble tau aggregates with a pathological conformation akin to the seed species used for templating. High content imaging revealed MC1+ insoluble aggregate filaments (Figure 2D), and quantification of aggregate area (Figure S2F) showed robust, concentration-dependent accumulation of these aggregates in seeded but not unseeded neurons (Figure 2E). Furthermore, aggregation was specific to tau and did not affect other microtubule-associated proteins such as MAP2 (Figures 2D and 2F). MAP2 also served as a measure of cell health, indicating that the exogenous seeds did not induce toxicity. In line with data reporting that tau aggregation is initiated in axons followed by mislocalization to the somatodendritic compartment (Devos et al, 2018), we did not observe 100% colocalization of MC1 and MAP2 (Figure 2D), which is found in dendrites and the soma.

To eliminate the possibility that the observed MC1+ aggregates represent residual exogenous seeds, tau aggregation was further evaluated in *MAPT*-KO hiPSC-neurons. CRISPR-Cas9 gene knockout resulting from indel formation (Chen and Pruett Miller, 2018; Cong et al, 2013; Mali et al, 2013) was confirmed by immunofluorescence and western blot analysis (Figures 2G and S2A), also showing no effect on the gross morphology and identity of the resulting hiPSC-neurons following differentiation (Figures S2B–S2C). In contrast to *MAPT*-WT neurons, no MC1+ insoluble tau was observed in *MAPT*-KO neurons 7 weeks following seeding (Figures 2D and 2E), suggesting that the MC1 signal detected in *MAPT*-WT neurons represents *de novo* aggregation that is dependent on endogenous tau expression.

Given that previous studies did not observe endogenous aggregation in *MAPT*-WT or *MAPT*-P301S/E10 + 16 hiPSC-neurons when seeded with truncated recombinant tau paired helical filaments (PHFs) (Verheyen et al, 2018), we further assessed whether our optimized differentiation platform and seeding with AD brain-derived tau could lead to aggregation in *MAPT*-P301S/E10 + 16 neurons. In contrast to the inhibitory outcome previously reported (Verheyen et al, 2018), *MAPT*-P301S/E10 + 16 neurons derived using the protocol described in Figure 1 showed expression of markers consistent with a cortical excitatory identity (Figures S2B and S2D). *MAPT-WT* neurons predominantly express the 0N3R tau isoform due to the developmental regulation of *MAPT* isoform expression and the immature status of the hiPSC-neurons (Brennand et al, 2015) except under extended culture periods >4 months (*data not shown*) (Miguel et al, 2019), whereas insertion of the intronic E10 + 16C > T mutation downstream of exon 10 has been shown to increase 4R splicing (Grover et al, 1999; Sposito et al, 2015), enabling expression of the P301S mutation (Figures 2G and 2H). Seven weeks post seeding with MC1-AD, *MAPT*-P301S/E10+16 neurons displayed concentration-dependent endogenous tau aggregation (Figures 2I and 2J). These data demonstrate that minimal concentrations of APTA-immunopurified AD tau species are sufficient to seed endogenous tau in hiPSC-derived excitatory cortical neurons without tau overexpression.

Endogenous tau aggregation can be achieved with a variety of AD brain-derived tau species

Because the MC1 antibody recognizes both early and late pathological tau forms that represent a mixture of soluble and insoluble species (Weaver et al, 2000), we next sought to determine whether sarkosyl-insoluble AD brain seeds (SI-AD) (Guo et al., 2016; Spillantini et al, 1998) could serve as a more potent inducer of

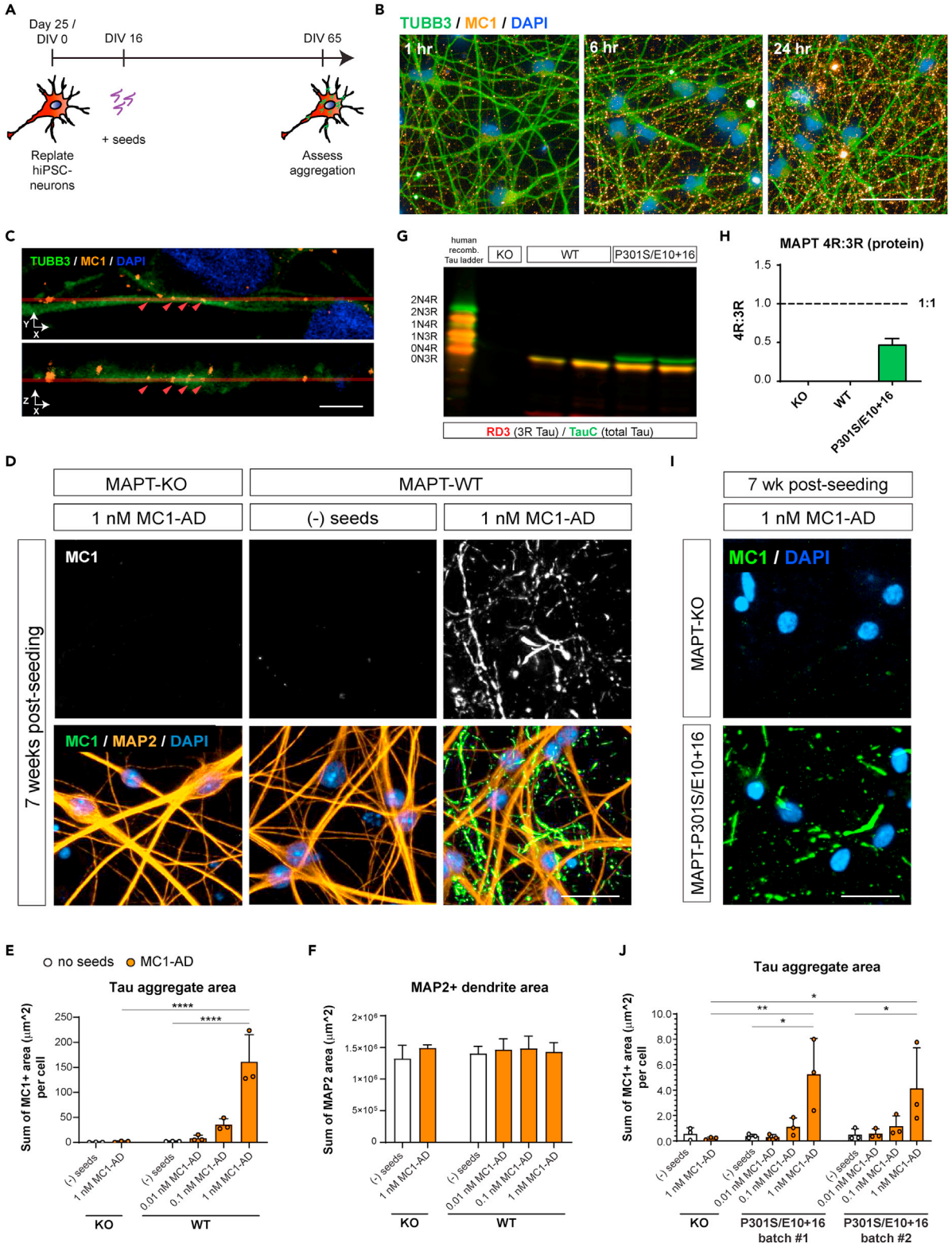

Figure 2. Tau aggregation in hiPSC-neurons does not require tau overexpression

(A) Tau aggregation assay timeline. Days *in vitro* (DIV) refers to the neuron maturation age in the final assay plate.

(B) Time-dependent increase of MC1 immunopurified AD brain-derived tau seeds (MC1-AD; yellow) seed co-localization with TUBB3+ (green) neurites.

Figure 2. *Continued*

(C) Confocal microscopy demonstrates association of MC1-AD seeds and colocalization within TUBB3+ neurites 24 h after seed addition.

(D) Representative IF images of methanol-insoluble MC1+ endogenous tau aggregations (white/green) in *MAPT*-WT but not *MAPT*-KO hiPSC-neurons 7 weeks after seeding with MC1-AD exogenous tau seeds. Nuclei labeled with DAPI (blue) and dendrites labeled with MAP2 (yellow).

(E) and (F) Quantification of MC1+ tau aggregate area per cell (E) or MAP2+ dendrite area (F) 7 weeks post seeding. Graphs represent mean +SD (n = 3 replicate wells, 30 fields per well). ****$p < 0.0001$ according to one-way ANOVA with Tukey's test comparing indicated conditions.

(G) Western blot analysis of 3R (RD3; red) and total tau (TauC; green) expression in phosphatase-treated lysates from DIV 21 *MAPT*-KO, *MAPT*-WT, and *MAPT*-P301S/E10 + 16 hiPSC-neurons. 3R bands are detected by both antibodies, displaying a yellow color due to overlap of signal, whereas 4R bands are only detected by the total tau antibody.

(H) TauC densitometry of the 4R band compared with the 3R band. Bar graph represents (mean +SD; n = 2 independent experiments).

(I) Representative IF images of *MAPT*-P301S/E10 + 16 hiPSC-neurons with methanol-insoluble MC1+ tau aggregates (green) 7 weeks post seeding with MC1-AD that are not observed in seeded *MAPT*-KO hiPSC-neurons. Nuclei labeled with DAPI (blue).

(J) Quantification of MC1+ tau aggregate area normalized to cell number. Graphs represent mean +SD (n = 3 replicate wells, 30 fields per well). *$p < 0.05$, **$p < 0.01$ according to one-way ANOVA with Tukey's test comparing indicated conditions. Scale bars: 50 μm (B); 10 μm (C); 25 μm (D, I). See also Figure S2.

tau aggregation in hiPSC-neurons. *MAPT*-WT neurons seeded with SI-AD resulted in significant MC1+ endogenous tau aggregation in a concentration-dependent manner 7 weeks post seeding (Figure 3A) in the absence of neurite toxicity (Figure S3A). Furthermore, in a head-to-head comparison SI-AD resulted in significantly higher levels of tau aggregation in just 5 weeks (Figures 3B and 3C), which could be reproduced in independently differentiated hiPSC-neurons (Figure S3B). MAPT-WT neurons seeded with SI-AD also demonstrated evidence of larger, perinuclear aggregates (Figure 3C, *arrow*), indicating a more advanced aggregation stage. Consistent with the idea that sarkosyl extraction isolates the competent tau species, the increased potency of SI-AD was also observed when compared with seeding with crude AD lysate (Figures S3C–S3D). In contrast, sarkosyl-insoluble material derived from non-AD/control donor brains (SI-C) had no effect on tau aggregation (Figures 3A–3C and S3B), demonstrating that templating was AD specific. Moreover, aggregation required endogenous expression of tau as no aggregation was observed in *MAPT*-KO neurons seeded with SI-AD or MC1-AD (Figures 3A–3C and S3B).

Assay optimization of tau seeding and aggregation

We next evaluated the timeline for seeding and amplification in order to determine the minimal assay window to achieve quantifiable aggregation for high-throughput applications (Figure 4A). We hypothesized that initiating templated assembly of native tau at an earlier stage of maturation prior to DIV 16 would reduce the total aggregation due to minimal co-firing activity (Figure S1E) and low tau expression (Figure S4A). Although *MAPT*-WT neurons seeded at DIV 7 exhibited a concentration-dependent increasing trend in MC1+ aggregates, the increase was not significant compared with unseeded neurons, indicating that seeding at DIV 16 significantly improves the signal window (Figure 4B). We next assessed whether the aggregation window could be shortened from 4 to 3 weeks. Significant endogenous aggregation was observed at both endpoints, with 4 weeks having more aggregates as expected (Figure 4B). Of note, MC1+ aggregates in the somatodendritic compartment after 3 or 4 weeks were rarely detected (Figure S4B), indicating that perinuclear localization represents a more advanced stage of aggregation that can only be observed with a longer incubation window as in Figure 3. Small, fibrillar structures resembling early aggregates could be visualized as early as 2 weeks post seeding in *MAPT*-WT neurons; however, this aggregation was not quantifiable owing to the high background signal displayed in *MAPT*-KO neurons (Figure 4C). The signal in *MAPT*-KO neurons decreased over time, suggesting that it could represent residual seeds that initially adhere to the surface of the neuronal culture (Figure 4C).

Given that the morphological and molecular changes accompanying the neurite network maturation could lead to greater seed uptake, accelerated assembly, and/or enhanced spreading in a shorter time frame, we also tested whether additional maturation prior to seeding would enhance the aggregation outcome. However, seeding at DIV 30 did not result in an aggregation outcome that exceeded the aggregation observed following seeding at DIV 16 when assessed in the same 44-day window (Figure 4B). Moreover, seeding at advanced maturation stages with longer incubation periods before the aggregation endpoint reduced endogenous aggregation (Figure S4C), suggesting that earlier seeding is optimal within this *in vitro* model system, which may decline over time due to other factors. These data demonstrate the importance of defining an appropriate minimal assay window that successfully balances neuronal maturity with the need to distinguish newly formed aggregates from exogenous tau seeds.

Using the optimized window and an independent extraction of SI-AD seeds, we further examined a wider dose range and multiple time points to determine whether tau aggregation impacted cell health. *MAPT*-

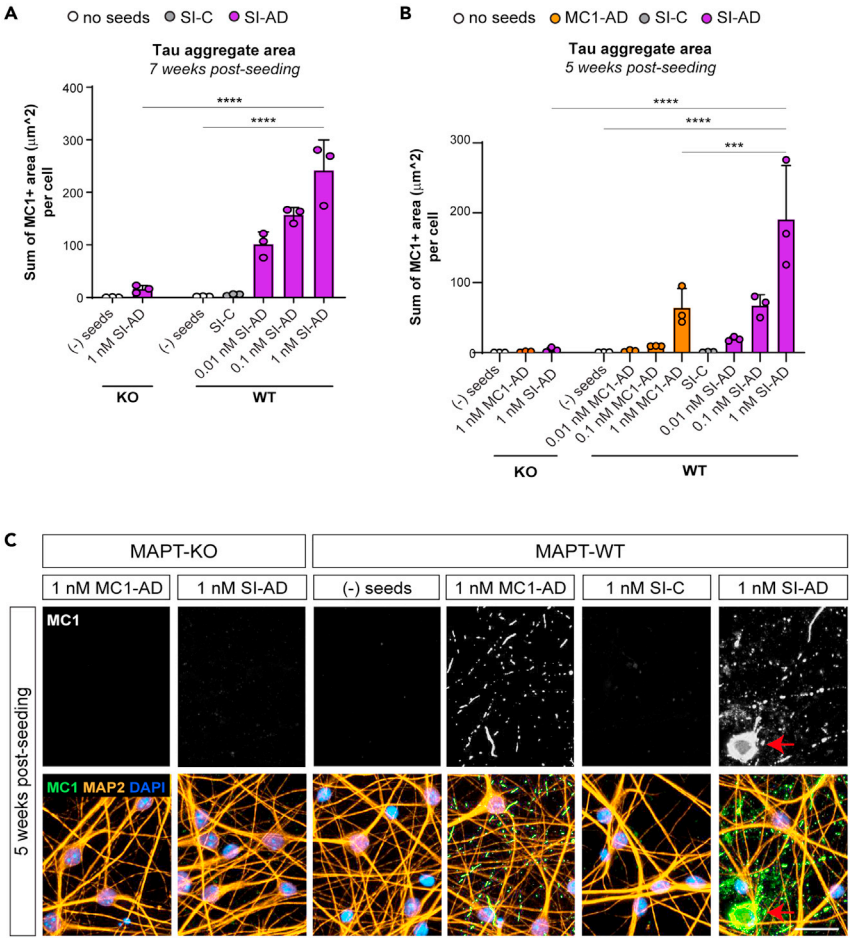

Figure 3. Increased seeding competency of sarkosyl-insoluble AD brain-derived tau in hiPSC-neurons

(A and B) Quantification of MC1+ aggregate area per cell 7 (A) or 5 weeks (B) post seeding shows concentration-dependent aggregation with MC1-AD or sarkosyl-insoluble AD brain seeds (SI-AD) but not sarkosyl-insoluble material from non-AD/control brains (SI-C). Graphs represent mean +SD (n = 3 replicate wells, 30 fields per well). ***$p < 0.001$, ****$p < 0.0001$ according to one-way ANOVA with Tukey's test comparing indicated conditions. SI-C volume matched to highest dose of SI-AD.

(C) Representative IF images of MC1+ endogenous tau aggregates in *MAPT*-WT hiPSC-neurons 5 weeks after addition of MC1-AD or sarkosyl-insoluble AD brain seeds (SI-AD) but not sarkosyl-insoluble material from non-AD/control brains (SI-C). Nuclei labeled with DAPI (blue) and dendrites labeled with MAP2 (yellow). Red arrow indicates aggregate localized to cell soma. Scale bar: 25 µm. See also Figure S3.

WT neurons demonstrated robust concentration-dependent tau aggregation that increased exponentially at 4 weeks but started to reach a plateau 7 weeks post seeding (Figures 4D and 4E). At either endpoint, no significant effect on cell number or dendrite area was observed (Figures 4D and 4E), mimicking the slow disease progression observed in patients.

Tau aggregation is dependent on the recipient tau and the seed species

Although expression of P301S 4R tau was not required for aggregation (Figure 2), the P301S mutation has been shown to increase the aggregation propensity of tau *in vitro* (Barghorn et al, 2000). To investigate whether aggregation is influenced by the recipient tau, we further edited the *MAPT*-P301S/E10 + 16 hiPSC line to include the E10 + 14C > T mutation (Figure 5A), enabling comparison of tau aggregation in hiPSC-neurons expressing 0N3R tau only (*MAPT*-WT) or mutant 0N4R > WT 0N3R (*MAPT*-P301S/E10+14/E10+16). Consistent with previous data (Hutton et al, 1998), the addition of the E10 + 14C > T intronic mutation further enhanced 4R tau expression and thus expression of the P301S mutation (Figure 5B). The hiPSC-neurons were seeded at DIV 16 and evaluated 4 weeks post seeding, unexpectedly revealing fewer, smaller

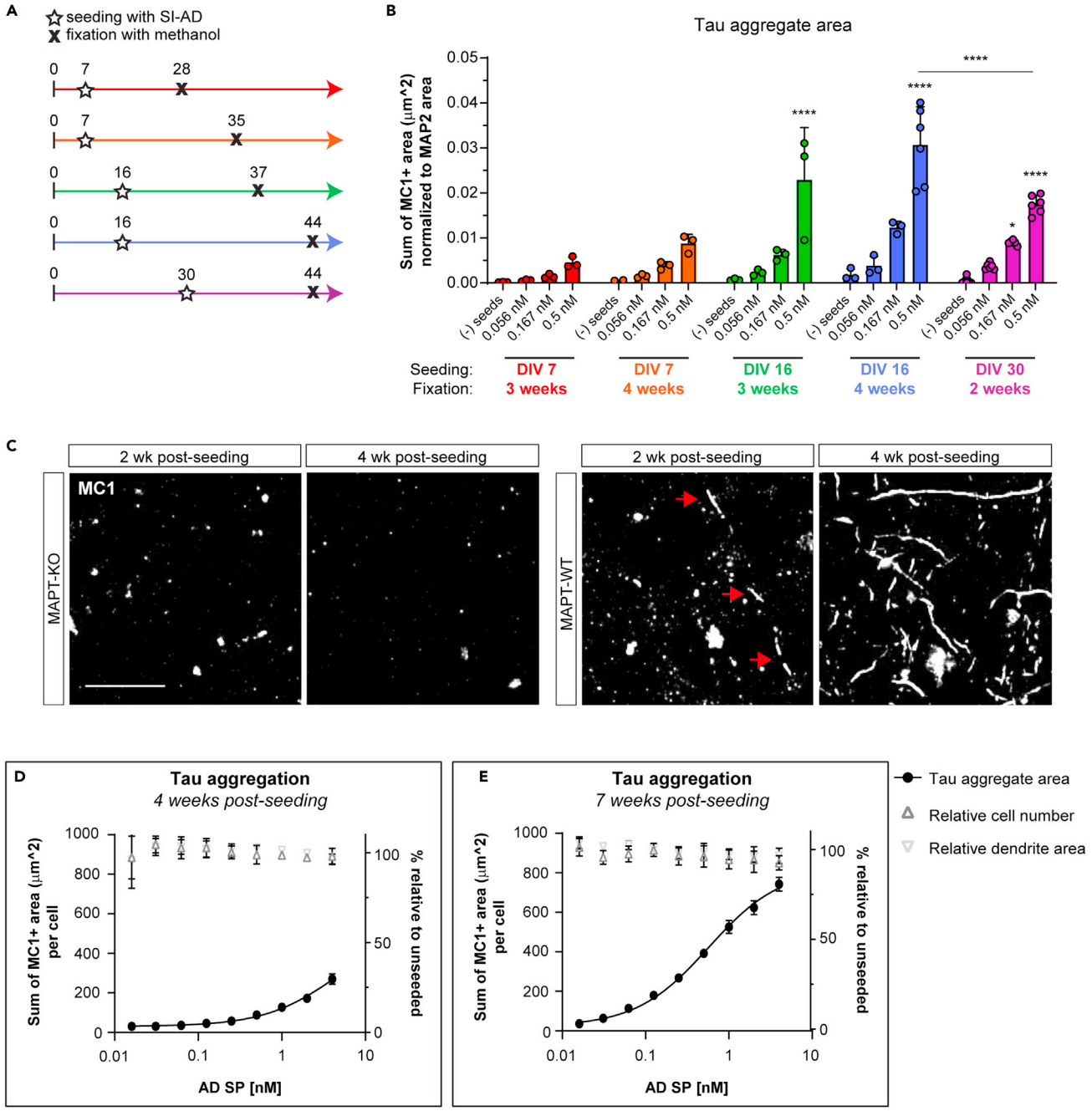

Figure 4. Timeline evaluation reveals optimal treatment and incubation windows for seeding, aggregation, and propagation and no effect on cell health

(A) Schematic of treatment timelines tested for addition of SI-AD seeds to *MAPT*-WT hiPSC-neurons. Numbers represent days of hiPSC-neuron maturation.

(B) Quantification of the area (μm^2) covered by insoluble, endogenous MC1+ aggregates relative to the MAP2 area using timelines described in (A). Graph represents mean +SD (n = 3 or 6 replicate wells, 30 fields per well). *p < 0.05, ****p < 0.0001 according to one-way ANOVA with Tukey's test comparing indicated condition to unseeded hiPSC-neurons.

(C) Representative IF images of MC1 immunoreactive material in *MAPT*-KO and *MAPT*-WT hiPSC-neurons treated with 0.5 nM SI-AD and fixed 2 or 4 weeks after seed addition. MC1 signal observed in the *MAPT*-KO likely represents residual seeds, which are diminished over time. Despite background signal at 2 weeks post seeding, filamentous aggregates are observed in *MAPT*-WT (arrowheads) and are further amplified by 4 weeks.

(D) and (E) Quantification of MC1+ aggregate area per cell 4 (D) or 7 weeks (E) post seeding with an independent extraction of SI-AD shows concentration-dependent aggregation in *MAPT*-WT neurons that increases between the two endpoints without reducing cell number (dark gray) or dendrite area (light gray). Graph represents mean ± SD (n = 3 replicate wells, 30 fields per well). Scale bar: 25 µm. See also Figure S4.

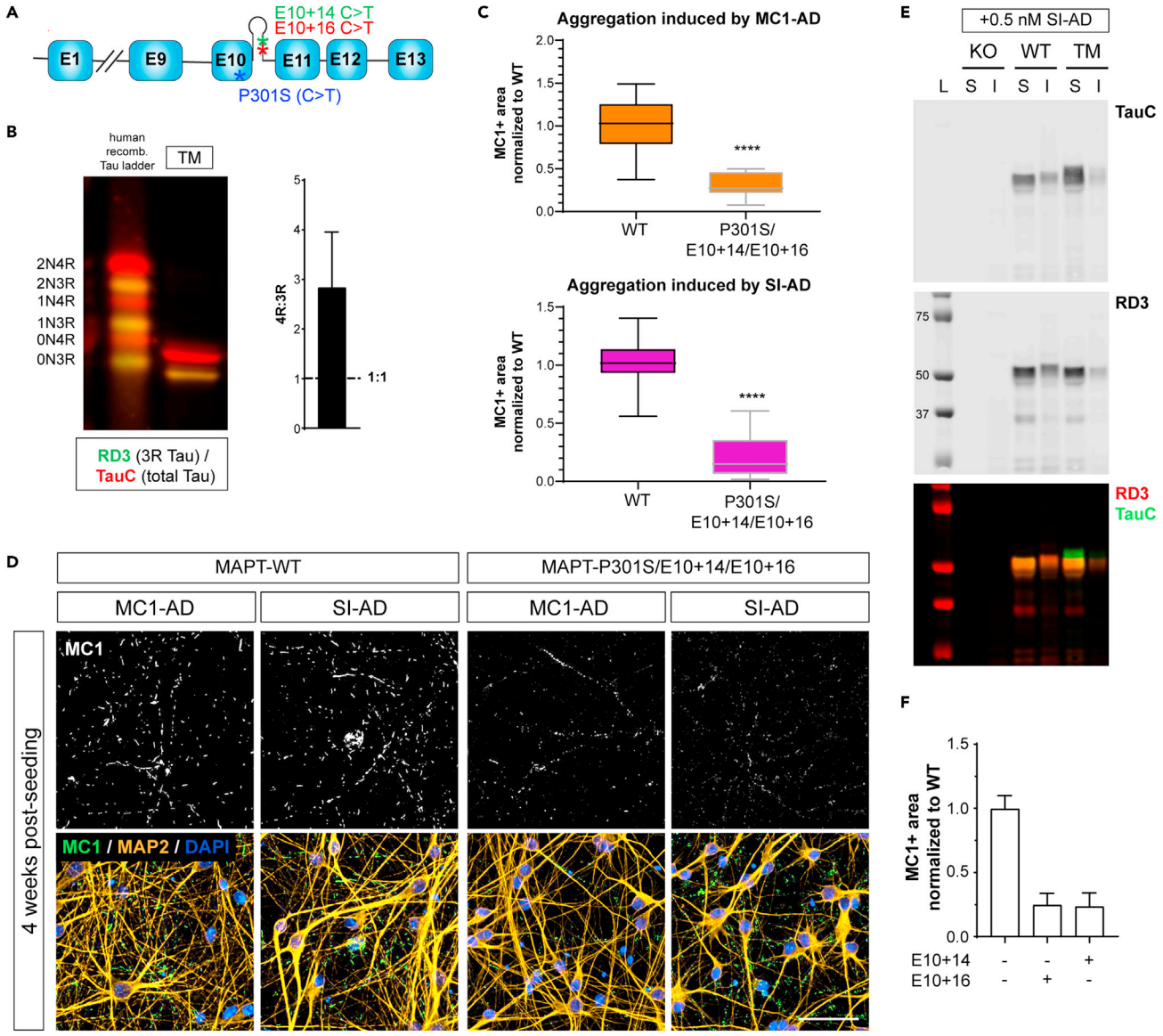

Figure 5. Endogenous tau aggregation in response to brain-derived seeds is influenced by the recipient tau expression

(A) Schematic depicting the *MAPT* locus and the location of the P301S, E10+14, and E10+16 mutations.

(B) Western blot analysis of phosphatase-treated lysates from *MAPT*-P301S/E10+14/E10+16 hiPSC-neurons (DIV 28). TauC densitometry shows that *MAPT*-P301S/E10+14/E10+16 express 4R > 3R. Graph represents mean +SD (n = 2 replicates).

(C) Quantification of MC1+ insoluble tau aggregate area in hiPSC-neurons treated with MC1-AD or SI-AD brain-derived seeds demonstrates reduced aggregation in *MAPT*-P301S/E10+14/E10+16 hiPSC-neurons regardless of seed concentration (0.01–1.5 nM). Graph represents mean +SD from independent seeding experiments where aggregation is normalized to the WT. ****$p < 0.0001$ according to Student's t test.

(D) Representative IF images depicting MC1+ aggregates in *MAPT*-WT and *MAPT*-P301S/E10 + 14/E10 + 16 hiPSC-neurons fixed 4 weeks after seeding with 1.5 nM MC1-AD or 0.6 nM SI-AD.

(E) Western blot analysis of total tau (TauC) and 3R tau (RD3) expression in sarkosyl-soluble (S) and sarkosyl-insoluble (I) protein extracts from *MAPT*-KO, *MAPT*-WT, and *MAPT*-P301S/E10+14/E10+16 (triple mutant; TM) hiPSC-neurons seeded with 0.5 nM SI-AD. L: protein ladder.

(F) Quantification of MC1+ insoluble tau aggregate area in isogenic hiPSC-neurons with different *MAPT* genotypes seeded with SI-AD. Bar graph represents mean +SD (n = 4 technical replicates from 2 independent experiments, 30 fields per well). See also Figure S5. Scale bar: 50 μm.

aggregates following seeding with either MC1-AD or SI-AD in *MAPT*-P301S/E10 + 14/E10 + 16 neurons compared with *MAPT*-WT neurons (Figures 5C and 5D). Sarkosyl extraction and biochemical analysis 4 weeks post seeding further demonstrated tau in the insoluble fraction in *MAPT-WT* neurons as well as higher-molecular-weight species not observed in the soluble fraction (Figure 5E). Consistent with the

immunofluorescence analysis, *MAPT*-P301S/E10 + 14/E10 + 16 neurons exhibited reduced insoluble tau (Figure 5E). Finally, *MAPT-KO* neurons showed no tau in either the soluble or insoluble fractions, confirming that the signals observed in the *MAPT*-WT and *MAPT*-P301S/E10+14/E10+16 neurons were not attributed to residual seeds (Figure 5E).

In order to determine whether the presence of the P301S mutation or the presence of increased 4R:3R contributed to the decrease in aggregation, we expanded our analysis to directly compare tau aggregation in isogenic hiPSC-neurons with biallelic editing at the *MAPT*-E10+16 or -E10+14 sites alone. These edits resulted in approximately 1:3 or 1:1 4R to 3R tau expression, respectively (Figure S5A). Assessment of insoluble tau aggregates 4 weeks post seeding showed that aggregation decreased with even the lowest expression of 4R tau in the absence of P301S (Figures 5F and S5B), indicating that the reduction in tau aggregation was not dependent on the mutant form of tau.

Several lines of evidence further suggest that tau aggregation may be influenced by the repeat domain makeup or mutation profile of the seed (Kaufman et al, 2016; Nonaka et al, 2010; Sanders et al, 2014; Strang et al, 2018; Yu et al, 2012). Therefore, we tested whether P301 mutant 4R tau would serve as a more appropriate template for aggregation in *MAPT*-P301S/E10+14/E10+16 neurons. Soluble monomeric 2N4R P301L tau was induced to form insoluble PHFs *in vitro* upon incubation with heparin (Goedert et al, 1996) (Figure S6A). Heparin-induced PHF demonstrated characteristic helical structures that can be broken down into smaller seeds upon sonication (Figures S6B and S6C). Four weeks post seeding, *MAPT*-P301S/E10+14/E10+16 neurons seeded with 10 nM 2N4R P301L sonicated PHF (sPHF) induced robust MC1+ aggregation (Figures 6A and 6B). In contrast, aggregates were absent in seeded *MAPT*-KO or 3R-expressing *MAPT*-WT neurons (Figures 6A and 6B). Evaluation of aggregation in response to 2N4R P301L sPHF in independently derived hiPSC-neuron batches consistently demonstrated aggregation in *MAPT*-P301S/E10 + 14/E10 + 16 but not *MAPT*-KO or *MAPT*-WT neurons (Figure S6D). In order to determine whether 2N4R P301L sPHF simply exhibits reduced aggregation kinetics in *MAPT*-WT neurons, the analysis was extended to 6 weeks post seeding, but no aggregation was observed (Figure 6A), suggesting incompatibility between the endogenous 3R wild-type tau and heparin-induced 2N4R mutant seeds. Moreover, sarkosyl extraction and biochemical analysis confirmed the presence of higher-molecular-weight tau species in the insoluble fraction in *MAPT-P301S/E10+14/E10+16* neurons but not *MAPT*-WT neurons (Figure 6C).

It was previously reported that P301L mutant tau cannot seed wild-type tau (Aoyagi et al, 2007). Therefore, we next examined whether heparin-induced 2N4R or 2N3R WT sPHF is seeding competent in neurons expressing WT tau. Given that templating may require repeat domain compatibility (Nonaka et al, 2010), analysis of WT sPHF was performed in isogenic *MAPT*-WT, *MAPT*-E10+14, and *MAPT*-P301S/E10+14/E10+16 hiPSC-neurons. As before, 2N4R P301L sPHF induced significant aggregation in *MAPT*-P301S/E10+14/E10+16 neurons. Seeding with 2N3R WT or 2N4R WT sPHFs also induced low-level, dose-dependent aggregation in *MAPT*-P301S/E10+14/E10+16 neurons, which was not significant compared with unseeded neurons (Figures 6D and S6E). Surprisingly, heparin-induced sPHF did not template aggregation in either *MAPT*-WT or *MAPT*-E10+14 neurons (Figures 6D and S6E), suggesting that repeat domain compatibility is not sufficient for templating. Nevertheless, these data demonstrate the ability to induce high levels of endogenous aggregation using low concentrations of heparin-induced recombinant PHFs when appropriately matched with *MAPT*-P301S/E10+14/E10+16 hiPSC-neurons.

Pathology-associated features of endogenous tau aggregates

Tau protein contains >85 potential sites for phosphorylation, which contribute to the pathological changes that occur in tauopathies (Goedert et al, 1989). Therefore, to validate the pathophysiological relevance of tau aggregation in seeded hiPSC-neurons, we evaluated whether the endogenous insoluble tau aggregates could also be labeled by phospho-specific antibodies. AT8, which recognizes pS202 and pT205, is associated with early stages of AD, whereas PHF1, which recognizes pSer396 and pS404, has been shown to associate with later stages of the disease (Bertrand et al, 2010) (Figure 7A). pS422 has been reported to be phosphorylated on synaptic tau (Collin et al, 2014) and may correlate with tau oligomerization (Ercan Herbst et al, 2019). In addition to MC1, AT8, PHF1, and pS422 recognized endogenous tau aggregates both in *MAPT*-WT neurons seeded with SI-AD (Figures 7B–7F) and in *MAPT*-P301S/E10+14/E10+16 neurons seeded with 2N4R P301L sPHF (Figures 7G–7K). Within our assay window, somatodendritic aggregates in *MAPT*-WT neurons were rare and showed immunoreactivity for MC1, whereas AT8, PHF1, or pS422 immunoreactivity was more limited to aggregates found in axons. In contrast, somatodendritic

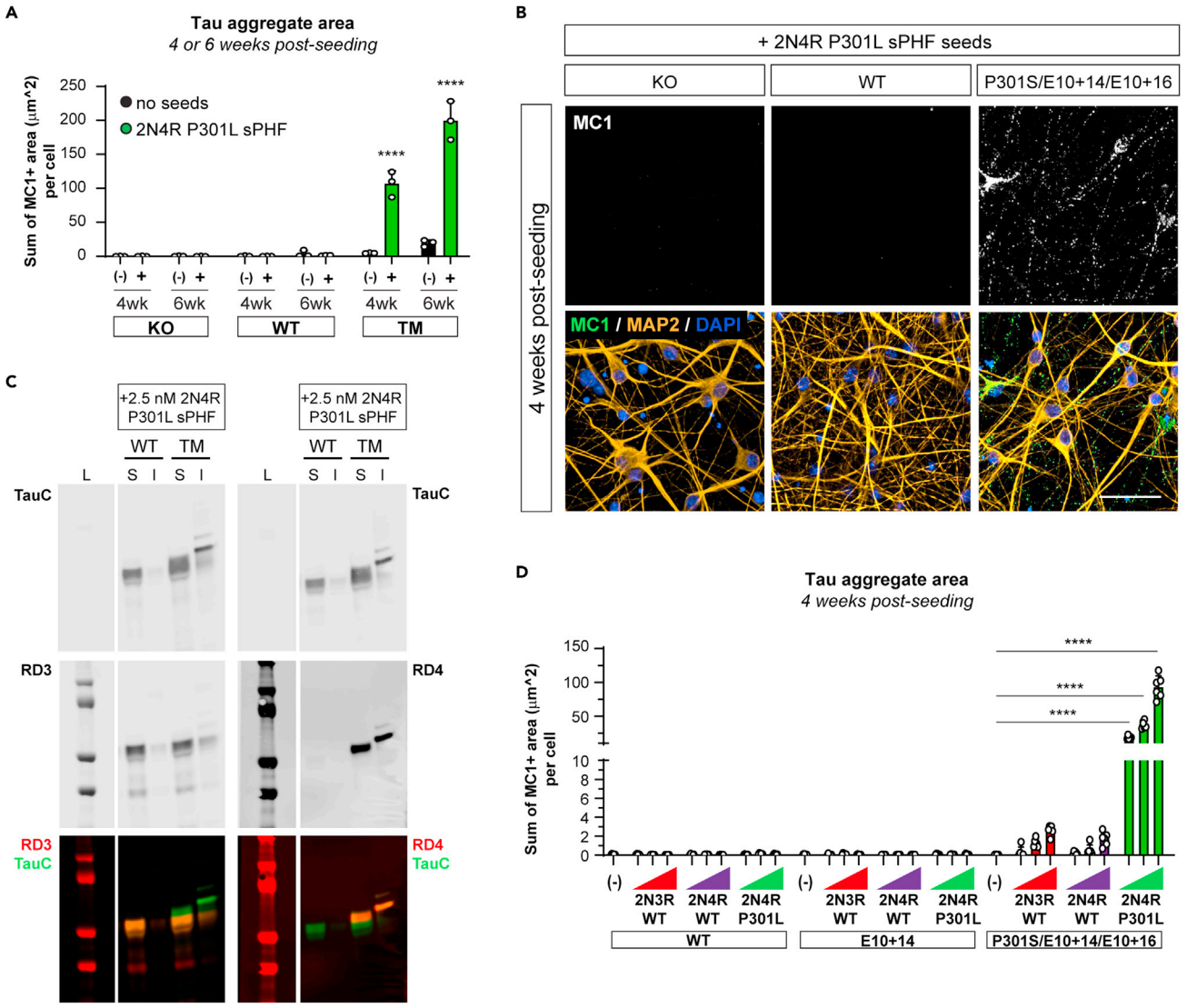

Figure 6. Heparin-induced recombinant tau seeds require mutant recipient tau for templating

(A) 10 nM 2N4R P301L recombinant tau sonicated paired helical filaments (sPHF) induce MC1+ tau aggregation in *MAPT*-P301S/E10+14/E10+16 (TM) but not *MAPT*-KO or *MAPT*-WT hiPSC-neurons 4 weeks post seeding. Extending the timeline to 6 weeks post seeding with 10 nM did not result in aggregation in *MAPT*-KO or *MAPT*-WT hiPSC-neurons. Graph represents mean MC1+ tau aggregate area per cell +SD (n = 3 replicate wells, 30 fields per well). ****$p < 0.0001$ according to three-way ANOVA with Tukey's test comparing indicated condition to unseeded hiPSC-neurons.

(B) Representative IF images depicting MC1+ aggregates in *MAPT*-P301S/E10+14/E10+16 but not *MAPT*-KO or *MAPT*-WT hiPSC-neurons fixed 4 weeks after seeding with 10 nM 2N4R P301L sPHF.

(C) Western blot analysis of total tau (TauC) and isoform-specific (RD3, RD4) expression in sarkosyl-soluble (S) and sarkosyl-insoluble (I) protein extracts from *MAPT*-WT and -P301S/E10+14/E10+16 (triple mutant; TM) hiPSC-neurons seeded with 2.5 nM 2N4R P301L sPHF.

(D) Quantification of MC1+ insoluble tau aggregate area per cell in *MAPT*-WT, -E10+14, or -P301S/E10+14/E10+16 hiPSC-neurons treated with heparin-induced sPHF. Graph represents mean +SD (n = 6 replicate wells, 16 fields per well). ****$p < 0.0001$ according to two-way ANOVA with Tukey's test comparing indicated condition to unseeded hiPSC-neurons. Scale bar: 50 µm. See also Figure S6.

aggregates were more prevalent in *MAPT*-P301S/E10+14/E10+16 neurons and showed immunoreactivity for AT8, PHF1, and pS422, suggesting that the aggregation kinetics in this model are accelerated.

To confirm their pathological relevance, endogenous tau aggregates in lysates from seeded hiPSC-neurons were also measured biochemically via homogeneous time resolved fluorescence (HTRF) (Degorce et al, 2009), a fluorescence resonance energy transfer (FRET) sandwich immunoassay, which utilizes a monoclonal tau antibody that recognizes aggregates in AD, but not control, brain tissue (Figure 7L). The HTRF

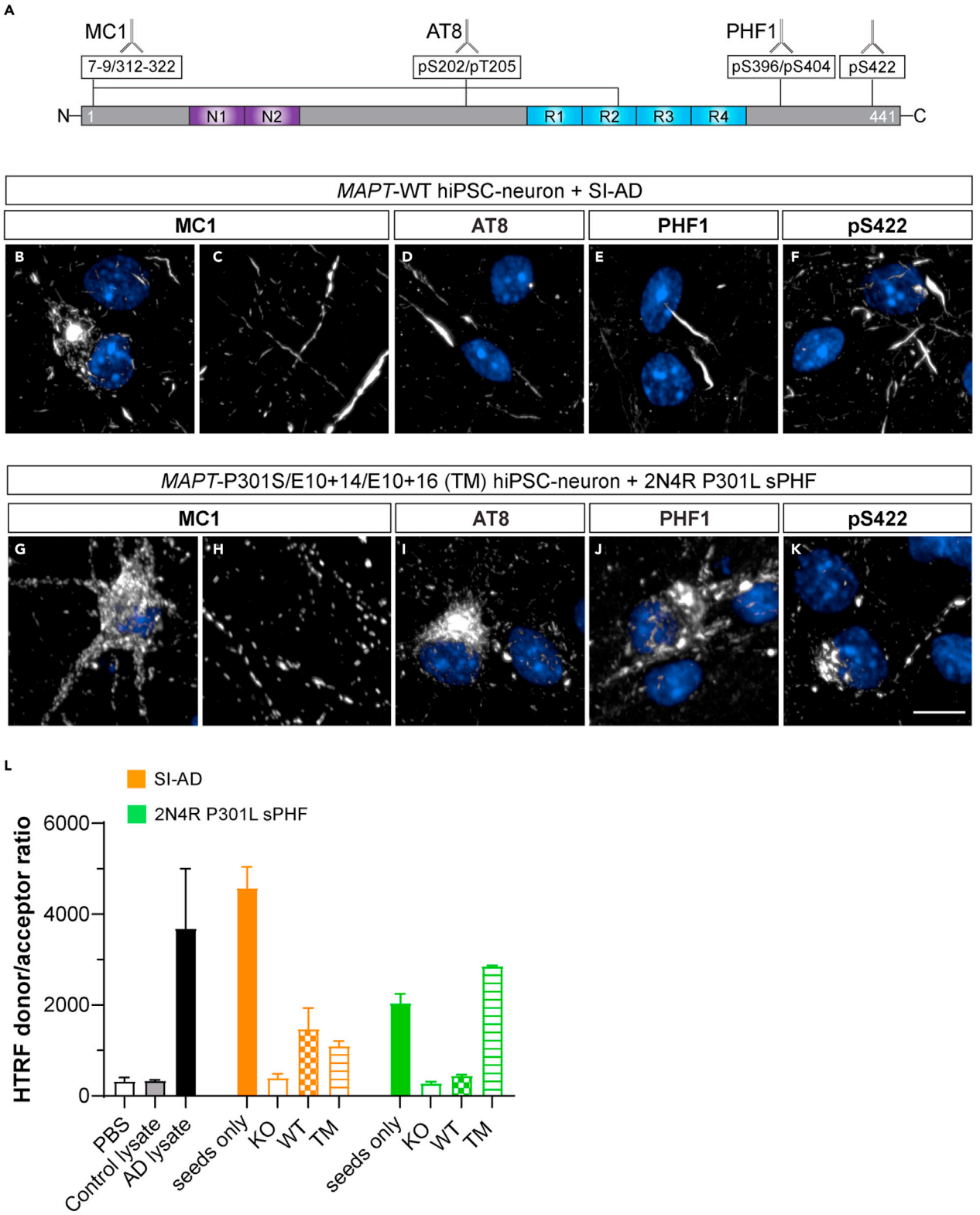

Figure 7. Endogenous tau aggregates in hiPSC-neurons display characteristic features of pathological tau

(A) Schematic diagram of tau protein domains and antibody-binding sites for MC1, AT8, PHF1, and pS422.

(B–K) Representative IF images showing immunoreactivity of endogenous tau aggregates in *MAPT*-WT hiPSC-neurons seeded with 0.5 nM SI-AD and in *MAPT*-P301S/E10+14/E10+16 hiPSC-neurons seeded with 2N4R P301L sPHF for MC1 (B, C, G, H), AT8 (D, I), PHF1 (E, J), and pS422 (F, K). (L) Biochemical

Figure 7. *Continued*
analysis using homogeneous time resolved fluorescence (HTRF) and a monoclonal tau antibody that specifically recognizes tau aggregates found in AD brain lysate, brain-derived (SI-AD) and recombinant (2N4R P301L sPHF) tau seeds. HTRF detects tau aggregates found in conditions that produced detectable aggregation by MC1 immunofluorescence but not in controls, which display a signal similar to background (PBS) or control brain lysate. Graph represents mean +SD (n = 2 technical replicates). Scale bar: 10 μm.

assay recognized both SI-AD and 2N4R P301L sPHF tau seeds (Figure 7L). In contrast to the seeds alone, *MAPT*-KO neurons seeded with SI-AD or 2N4R P301L sPHF did not display aggregation by HTRF, whereas *MAPT*-WT and *MAPT*-P301S/E10+14/E10+16 neurons seeded with SI-AD or 2N4R P301L sPHF, respectively, displayed a significant signal over background (Figure 7L). Furthermore, absence of HTRF signal in *MAPT*-WT neurons seeded with 2N4R P301L sPHF and reduced signal in *MAPT*-P301S/E10 + 14/E10 + 16 neurons paralleled their relative MC1 immunofluorescence readouts. Taken together, these data confirm the ability of this human neuron *in vitro* model to recapitulate relevant pathological features associated with tau aggregation.

DISCUSSION

In this study we determined the minimal requirements for endogenous tau aggregation in hiPSC-neurons in order to define a more physiologically relevant model system for studying tau pathobiology. Of importance, standardization of the protocol using quality control measures to define successful differentiations enabled robust and reproducible generation of excitatory cortical neurons. Given that cell density changes during the early stages of the differentiation are sufficient to shift the cell fate from the central nervous system to peripheral nervous system (Chambers et al, 2009), it was critical to monitor the presence of Sox10+ neural crest. Minimizing the contamination of AP2α+/SOX10-non-neural ectoderm fates early on also helped to eliminate the appearance of commonly observed flat, proliferating cells that can arise in response to high Wnt levels and take over the hiPSC-neurons (*data not shown*). We also defined a minimal γ-secretase inhibitor treatment window to induce the differentiation of NPCs to neurons without permanently affecting APP processing, which may contribute to pathology in an AD hiPSC-neuron model. Lastly, we found that it was important to optimize the microwell plate coating procedure and plating density to sustain the health of the hiPSC-neurons and maintain a uniform neuron distribution without the clustering that often plagues long-term hiPSC-neuron cultures. Using this platform, we consistently achieved the desired neuronal identity as compared with recent publications suggesting an inhibitory bias of the differentiation (Verheyen et al, 2018) when using BMP and TGFβ inhibition alone (Shi et al, 2012) and ensured that each batch of hiPSC-neurons implemented in downstream tau aggregation experiments met these criteria.

We defined assay windows that appropriately captured the desired biology within a reasonable time frame. Functional assessment of the hiPSC-neurons indicated that a minimum of 2 weeks of maturation was required for the co-firing activity that signifies a connected network. Furthermore, the minimal maturation time required for tau protein expression indicated that *MAPT* RNA expression ramps up very quickly following hiPSC-neuron re-plating, whereas tau protein expression requires >1 week. These features associated with the maturation of the neuronal culture may have contributed to the decreased aggregation observed following seeding at DIV 7 compared with DIV 16, indicating that there is less tau around at earlier timepoints and thus a reduced pool that can undergo fibrillization.

Endogenous tau aggregation was achieved in cell lines expressing 0N3R WT or 0N3R WT/0N4R P301S tau, which does not require overexpression of mutant tau. These results are in contrast to previously published studies that measured small oligomers using AlphaLISA but were unable to demonstrate insoluble tau aggregates even in the presence of overexpressed or endogenous pro-aggregation mutations in hiPSC-neurons (García León et al, 2018; Verheyen et al, 2015; Verheyen et al, 2018). Based on our findings, the use of recombinant tau seeds containing only the RD domain in those studies may not be compatible with their hiPSC-neurons. Furthermore, the high concentrations of tau seeds that were implemented (>50 nM) may have impeded or masked any endogenous tau aggregation. Confidence in the aggregation outcome was achieved in part by implementing appropriate controls. Adding seeds to *MAPT*-KO hiPSC-neurons enabled us to distinguish residual tau seeds and newly formed aggregates. Comparison of MC1 staining in tau-expressing hiPSC-neurons to *MAPT*-KO hiPSC-neurons demonstrated that the aggregates were dependent on endogenous tau expression. Important, all experiments presented here showed increasing aggregation with increasing dose while still maintaining neuronal survival. In addition, the absence of

aggregation in response to sarkosyl insoluble material derived from non-AD brains further indicates that endogenous tau aggregation is induced by an AD-specific component.

We show that AD brain-derived seeds induce more aggregation in 0N3R expressing *MAPT*-WT neurons than in neurons expressing both 3R and 4R isoforms. Similarly, recent work from He et al. indicates that AD brain lysate containing 3R and 4R tau induces more aggregation in mice expressing 3R than in mice expressing 4R (He et al, 2020). Adams et al. also showed that even small amounts of 3R can significantly decrease 4R assembly *in vitro* (Adams et al, 2010), which may explain why the total aggregation decreases as 4R expression increases in our model. Alternatively, the observed difference may be due to availability of tau, which is likely decreased in hiPSC-neurons expressing 4-repeat tau due to enhanced binding to microtubules. Although we tested multiple preparations of SI-AD and observed a consistent outcome, recently reported patient-specific differences observed in HEK cell and primary neuron seeding models (Dujardin et al, 2020) could also contribute to this phenomenon, indicating that future analysis of SI-AD seeding from individual patients will be important to provide additional understanding.

We also demonstrated that while heparin-induced tau PHF is capable of triggering tau aggregation in *MAPT*-P301S/E10+14/E10+16 neurons, they are incompatible with neurons expressing wild-type tau. Furthermore, the aggregation initiated by heparin-induced tau PHF in *MAPT*-P301S/E10+14/E10+16 neurons significantly decreases with WT compared with P301L seeds. Indeed, immuno- and cryo-EM studies have shown that brain-derived tau aggregates from AD and Pick's disease differ from each other as well as from heparin-induced 3R or 4R PHF (Zhang et al, 2019); however, these comparisons have yet to be made with the structure of 4R tau found in corticobasal degeneration (Zhang et al, 2020), which may show similarity to our P301S model. Nonetheless, the recent work from He et al. also suggests that aggregation is influenced by the disease origin of the seed rather than its repeat domain makeup (He et al, 2020). These data hint at cross-seeding barriers that speak to conformation-specific properties, which may explain the specificity of compatibility observations in the hiPSC-neuron models.

Lastly, the endogenous tau aggregates found in the hiPSC-neurons demonstrated several characteristics consistent with pathological tau found in human neurodegenerative diseases. In addition to representing insoluble tau not removed by methanol fixation, the endogenous tau aggregates were also found to be sarkosyl insoluble and of a higher molecular weight, indicating hyperphosphorylation. We also detected immunoreactivity using antibodies that recognize not only pathological conformations of tau (MC1) but also phosphorylation sites associated with the hyperphosphorylation observed in tauopathies (AT8, PHF1, pS422). The tau aggregates found in our hiPSC-neurons could also be measured using a commercially available biochemical assay. Additional time course evaluation will be required to further dissect the phosphorylation hierarchy and kinetics.

Limitations of the study

It is important to note that this hiPSC-neuron model still possesses limitations. The molecular age of hiPSC-neurons does not align with the donor age resulting from a reset that occurs during reprogramming (Mertens et al, 2015;Miller et al, 2013). As such, hiPSC-neurons cannot replicate all aspects of neurons that would be found in an aged adult when AD typically presents, including expression of all six isoforms of tau that can be found in patients with NFT in AD with 3R and 4R tau at a 1:1 ratio (Buée et al, 2000). Using current protocols, tau expression in *MAPT*-WT hiPSC-neurons is initially limited to the 0N3R isoform, and although extended time frames and alternative medias (Miguel et al, 2019) can result in expression of additional isoforms, these timelines are impractical for high-throughput analyses. Fortunately, we and others (Grover et al, 1999; Sposito et al, 2015; bib_Verheyen et al, 2018) have shown that gene editing enables the insertion of non-coding mutations that artificially increase 0N4R expression in hiPSC-neurons using intronic mutations. In the future, it will be interesting to further explore strategies aimed at altering exon 2/3 splicing as well to achieve 1N expression, which would improve the physiological relevance of the model given the high abundance of 1N isoforms in AD (Goedert and Jakes, 1990).

Another limitation worth mentioning is the lack of a pan-neurite antibody compatible with methanol fixation. MAP2 was utilized here as a marker of cell health as well as a microtubule-associated protein not affected by seeding. However, MAP2, which is found in the soma and dendrites, is not expected to colocalize with tau aggregates during early phases of aggregation when tau is hyperphosphorylated and

released from microtubules. Although controls were used throughout this study successfully demonstrating *de novo* aggregation, a pan-neurite antibody would provide further confidence.

We showed that a variety of heparin-induced 2N3R and 2N4R recombinant tau PHFs are incompatible with MAPT-WT hiPSC-neurons, whereas we did not test whether isoform-matched heparin-induced 0N3R recombinant Tau PHF would induce aggregation in our MAPT-WT hiPSC-neuron model. We suspect that this would not induce aggregation similar to 2N3R recombinant Tau sPHF, which would further suggest that the heparin-induced seed conformation is incompatible with hiPSC-neurons expression wild-type tau, but this would need to be validated in future studies.

Also of importance is that the tau aggregation model presented here exclusively addresses tau-centric, cell autonomous effects in neurons and does not examine the contribution of Aβ or non-neuronal cells such as astrocytes and microglia that may impact tau aggregation and spreading *in vivo*.

Conclusions

Combining well-characterized tau seed preparations and quality-controlled hiPSC-derived cortical neurons, we established a robust and reproducible tau aggregation model that demonstrates the specificity of tau aggregation and offers the ability to initiate endogenous tau aggregation using either brain-derived or recombinant tau seeds when combined with the appropriate *MAPT* genotype. The human neuronal model system coupled with the high content imaging workflow represents an advanced platform for evaluating clinically relevant antibodies against pathological tau and for identifying and validating physiologically relevant targets with a wide variety of treatment paradigms and extended culture times possible without cell loss. Most importantly, the induction of endogenous tau aggregation in human neurons using AD brain-derived competent tau species provides a new opportunity to evaluate physiological mechanisms of tau aggregation and propagation that may be unique to AD compared with other tauopathies.

STAR★METHODS

Detailed methods are provided in the online version of this paper and include the following:

- KEY RESOURCES TABLE
- RESOURCE AVAILABILITY
  - Lead contact
  - Materials availability
  - Data and code availability
- EXPERIMENTAL MODEL AND SUBJECT DETAILS
  - Human iPSC lines, culture, and MAPT editing
  - Brain tissue
- METHOD DETAILS
  - hiPSC differentiation to cortical neurons
  - Cell characterization immunofluorescence
  - Analysis of secreted Aβ
  - Calcium imaging
  - Brain-derived tau seeds
  - Recombinant tau seeds
  - Tau aggregation assay
  - Tau aggregation immunofluorescence
  - Fluorescence microscopy
  - Western blot analysis
  - HTRF
  - RNA isolation and quantitative PCR
- QUANTIFICATION AND STATISTICAL ANALYSIS

SUPPLEMENTAL INFORMATION

Supplemental information can be found online at https://doi.org/10.1016/j.isci.2021.103658.

ACKNOWLEDGMENTS

Special thanks to Peter Davies of Feinstein Institute who passed away during the preparation of this manuscript for providing MC1 and CP27 antibodies as well as MC1 immunopurified AD seeds, which have been invaluable to tau research. These reagents were received through a Material Transfer Agreement. We would like to thank the Massachusetts Alzheimer's Disease Research Center for donated AD and non-AD brain tissue (funded by grant P50 AG005134). We would also like to thank Washington University in St. Louis Genome Engineering and iPSC Center for performing gene editing (funded by Abbvie). We thank Abbvie employees Heyne Lee, Haiyan Wu, and Vivek Gautam for providing reagents and protocols and Sharvani Vodnala (Abbvie) and Julia Ennis, Julia Kushakji, Brianna Hilton, Miwei Hu, and Lilly Ryll (former Abbvie employees at the time of the study) for characterizing reagents and optimizing protocols. Financial support for this research was provided by AbbVie.

AUTHOR CONTRIBUTIONS

Conceptualization, J.D.M. and X.L.; methodology, J.D.M., C.N.P., P.R., K.T., and J.W.; validation, C.N.P., P.R., and T.K.; investigation, J.D.M., C.N.P., N.V., J.T., T.K., and A.D.W.; resources, T.K., K.Y., and T.R.J.; writing – original draft, J.D.M.; writing – review & editing, all authors; visualization, J.D.M., C.N.P., N.V., J.T., T.K., T.R.J., and A.D.W.; supervision, X.L. and E.K.; project administration, J.D.M.; funding acquisition, X.L. and E.K.

DECLARATION OF INTERESTS

J.D.M., C.N.P., N.V., P.R., T.K., K.Y., E.K., and X.L. are employees of AbbVie. A.D.W., J.T., K.T., and T.R.J. were employees of AbbVie at the time of the study. The design, study conduct, and financial support for this research were provided by AbbVie. AbbVie participated in the interpretation of data, review, and approval of the publication.

Received: February 10, 2021
Revised: April 27, 2021
Accepted: December 13, 2021
Published: January 21, 2022

REFERENCES

Adams, S.J., Deture, M.A., Mcbride, M., Dlckson, D.W., and Petrucelli, L. (2010). Three repeat isoforms of tau inhibit assembly of four repeat tau filaments. PloS one *5*, e10810.

Allsopp, T.E., Ebneth, A., and Cabrera-Socorro, A. (2019). Deploying human pluripotent stem cells to treat central nervous system disorders: facts, challenges and realising the potential. Stem Cell Res. *41*, 101581.

Aoyagi, H., Hasegawa, M., and Tamaoka, A. (2007). Fibrillogenic nuclei composed of P301L mutant tau induce elongation of P301L tau but not wild-type tau. J. Biol. Chem. *282*, 20309–20318.

Arriagada, P.V., Growdon, J.H., Hedley-Whyte, E.T., and Hyman, B.T. (1992). Neurofibrillary tangles but not senile plaques parallel duration and severity of Alzheimer's disease. Neurology *42*, 631–639.

Barghorn, S., Zheng-Fischhöfer, Q., Ackmann, M., Biernat, J., Von Bergen, M., Mandelkow, E.M., and Mandelkow, E. (2000). Structure, microtubule interactions, and paired helical filament aggregation by tau mutants of frontotemporal dementias. Biochemistry *39*, 11714–11721.

Bertrand, J., Plouffe, V., Sénéchal, P., and Leclerc, N. (2010). The pattern of human tau phosphorylation is the result of priming and feedback events in primary hippocampal neurons. Neuroscience *168*, 323–334.

Borghese, L., Dolezalova, D., Opitz, T., Haupt, S., Leinhaas, A., Steinfarz, B., Koch, P., Edenhofer, F., Hampl, A., and Brüstle, O. (2010). Inhibition of notch signaling in human embryonic stem cell-derived neural stem cells delays G1/S phase transition and accelerates neuronal differentiation in vitro and in vivo. Stem Cells *28*, 955–964.

Braak, H., and Braak, E. (1991). Neuropathological stageing of Alzheimer-related changes. Acta Neuropathol. *82*, 239–259.

Brennand, K., Savas, J.N., Kim, Y., Tran, N., Simone, A., Hashimoto-Torii, K., Beaumont, K.G., Kim, H.J., Topol, A., Ladran, I., et al. (2015). Phenotypic differences in hiPSC NPCs derived from patients with schizophrenia. Mol. Psychiatry *20*, 361–368.

Brunden, K.R., Trojanowski, J.Q., and Lee, V.M. (2009). Advances in tau-focused drug discovery for Alzheimer's disease and related tauopathies. Nat. Rev. Drug Discov. *8*, 783–793.

Buée, L., Bussière, T., Buée-Scherrer, V., Delacourte, A., and Hof, P.R. (2000). Tau protein isoforms, phosphorylation and role in neurodegenerative disorders. Brain Res. Brain Res. Rev. *33*, 95–130.

Cao, S.-Y., Hu, Y., Chen, C., Yuan, F., Xu, M., Li, Q., Fang, K.-H., Chen, Y., and Liu, Y. (2017). Enhanced derivation of human pluripotent stem cell-derived cortical glutamatergic neurons by a small molecule. Scientific Rep. *7*, 3282.

Chambers, S.M., Fasano, C.A., Papapetrou, E.P., Tomishima, M., Sadelain, M., and Studer, L. (2009). Highly efficient neural conversion of human ES and iPS cells by dual inhibition of SMAD signaling. Nat. Biotechnol. *27*, 275–280.

Chang, C.-W., Shao, E., and Mucke, L. (2021). Tau: Enabler of diverse brain disorders and target of rapidly evolving therapeutic strategies. Science *371*, eabb8255.

Chen, Y.-H., and Pruett-Miller, S.M. (2018). Improving single-cell cloning workflow for gene editing in human pluripotent stem cells. Stem Cell Res. *31*, 186–192.

Collin, L., Bohrmann, B., Göpfert, U., Oroszlan-Szovik, K., Ozmen, L., and Grüninger, F. (2014). Neuronal uptake of tau/pS422 antibody and reduced progression of tau pathology in a mouse model of Alzheimer's disease. Brain *137*, 2834–2846.

Cong, L., Ran, F.A., Cox, D., Lin, S., Barretto, R., Habib, N., Hsu, P.D., Wu, X., Jiang, W., Marraffini, L.A., and Zhang, F. (2013). Multiplex genome

engineering using CRISPR/Cas systems. Science *339*, 819–823.

Degorce, F., Card, A., Soh, S., Trinquet, E., Knapik, G.P., and Xie, B. (2009). Htrf: a technology tailored for drug discovery a review of theoretical aspects and recent applications. Curr. Chem. Genomics *3*, 22–32.

Devos, S.L., Corjuc, B.T., Oakley, D.H., Nobuhara, C.K., Bannon, R.N., Chase, A., Commins, C., GONZALEZ, J.A., Dooley, P.M., Frosch, M.P., and Hyman, B.T. (2018). Synaptic tau seeding precedes tau pathology in human Alzheimer's disease brain. Front. Neurosci. *12*.

Dujardin, S., Commins, C., Lathuiliere, A., Beerepoot, P., Fernandes, A.R., Kamath, T.V., De Los Santos, M.B., Klickstein, N., Corjuc, D.L., Corjuc, B.T., et al. (2020). Tau molecular diversity contributes to clinical heterogeneity in Alzheimer's disease. Nat. Med. *26*, 1256–1263.

Ercan-Herbst, E., Schöndorf, D.C., Behrendt, A., Klaus, B., Ramos, B.G., Weber, C., and Ehrnhoefer, D.E. (2019). A Post-translational modification signature defines changes in soluble Tau correlating with oligomerization in early stage Alzheimer's disease brain. bioRxiv, 594820.

Fu, H., Hardy, J., and Duff, K.E. (2018). Selective vulnerability in neurodegenerative diseases. Nat. Neurosci. *21*, 1350–1358.

García-León, J.A., Cabrera-Socorro, A., Eggermont, K., Swijsen, A., Terryn, J., Fazal, R., Nami, F., Ordovás, L., Quiles, A., Lluis, F., et al. (2018). Generation of a human induced pluripotent stem cell-based model for tauopathies combining three microtubule-associated protein TAU mutations which displays several phenotypes linked to neurodegeneration. Alzheimers Dement *14*, 1261–1280.

Gaspard, N., Bouschet, T., Hourez, R., Dimidschstein, J., Naeije, G., Van Den Ameele, J., Espuny-Camacho, I., Herpoel, A., Passante, L., Schiffmann, S.N., et al. (2008). An intrinsic mechanism of corticogenesis from embryonic stem cells. Nature *455*, 351–357.

Goedert, M., and Jakes, R. (1990). Expression of separate isoforms of human tau protein: correlation with the tau pattern in brain and effects on tubulin polymerization. Embo j *9*, 4225–4230.

Goedert, M., Jakes, R., Spillantini, M.G., Hasegawa, M., Smith, M.J., and Crowther, R.A. (1996). Assembly of microtubule-associated protein tau into Alzheimer-like filaments induced by sulphated glycosaminoglycans. Nature *383*, 550–553.

Goedert, M., Spillantini, M.G., Jakes, R., Rutherford, D., and Crowther, R.A. (1989). Multiple isoforms of human microtubule-associated protein tau: sequences and localization in neurofibrillary tangles of Alzheimer's disease. Neuron *3*, 519–526.

Grover, A., Houlden, H., Baker, M., Adamson, J., Lewis, J., Prihar, G., Pickering-Brown, S., Duff, K., and Hutton, M. (1999). 5' splice site mutations in tau associated with the inherited dementia FTDP-17 affect a stem-loop structure that regulates alternative splicing of exon 10. J. Biol. Chem. *274*, 15134–15143.

Guo, J.L., and Lee, V.M. (2011). Seeding of normal Tau by pathological Tau conformers drives pathogenesis of Alzheimer-like tangles. J. Biol. Chem. *286*, 15317–15331.

Guo, J.L., Narasimhan, S., Changolkar, L., He, Z., Stieber, A., Zhang, B., Gathagan, R.J., Iba, M., Mcbride, J.D., Trojanowski, J.Q., and Lee, V.M. (2016). Unique pathological tau conformers from Alzheimer's brains transmit tau pathology in nontransgenic mice. J. Exp. Med. *213*, 2635–2654.

Hansen, D.V., Rubenstein, J.L., and Kriegstein, A.R. (2011). Deriving excitatory neurons of the neocortex from pluripotent stem cells. Neuron *70*, 645–660.

He, Z., Mcbride, J.D., Xu, H., Changolkar, L., Kim, S.-J., Zhang, B., Narasimhan, S., Gibbons, G.S., Guo, J.L., Kozak, M., et al. (2020). Transmission of tauopathy strains is independent of their isoform composition. Nat. Commun. *11*, 7.

Hiller, B.M., Marmion, D.J., Gross, R.M., Thompson, C.A., Chavez, C.A., Brundin, P., Wakeman, D.R., Mcmahon, C.W., and Kordower, J.H. (2020). Mitomycin-C treatment during differentiation of induced pluripotent stem cell-derived dopamine neurons reduces proliferation without compromising survival or function invivo. Stem Cells Transl Med *10*, 278–290.

Hutton, M., Lendon, C.L., Rizzu, P., Baker, M., Froelich, S., Houlden, H., Pickering-Brown, S., Chakraverty, S., Isaacs, A., Grover, A., et al. (1998). Association of missense and 5'-splice-site mutations in tau with the inherited dementia FTDP-17. Nature *393*, 702–705.

Jicha, G.A., Bowser, R., Kazam, I.G., and Davies, P. (1997). Alz-50 and MC-1, a new monoclonal antibody raised to paired helical filaments, recognize conformational epitopes on recombinant tau. J. Neurosci. Res. *48*, 128–132.

Kaufman, S.K., Sanders, D.W., Thomas, T.L., Ruchinskas, A.J., Vaquer-Alicea, J., Sharma, A.M., Miller, T.M., and Diamond, M.I. (2016). Tau prion strains dictate patterns of cell pathology, progression rate, and regional vulnerability in vivo. Neuron *92*, 796–812.

Lim, S., Haque, M.M., Kim, D., Kim, D.J., and Kim, Y.K. (2014). Cell-based models to investigate tau aggregation. Comput. Struct. Biotechnol. J. *12*, 7–13.

Mali, P., Yang, L., Esvelt, K.M., Aach, J., Guell, M., Dicarlo, J.E., NORVILLE, J.E., and CHURCH, G.M. (2013). RNA-guided human genome engineering via Cas9. Science *339*, 823–826.

Mandelkow, E.-M., and Mandelkow, E. (1998). Tau in Alzheimer's disease. Trends Cell Biol. *8*, 425–427.

Medda, X., Mertens, L., Versweyveld, S., Diels, A., Barnham, L., Bretteville, A., Buist, A., Verheyen, A., Royaux, I., Ebneth, A., and Cabrera-Socorro, A. (2016). Development of a scalable, high-throughput-compatible assay to detect tau aggregates using iPSC-derived cortical neurons maintained in a three-dimensional culture format. J. Biomol. Screen *21*, 804–815.

Mertens, J., Paquola, A.C.M., Ku, M., Hatch, E., Böhnke, L., Ladjevardi, S., Mcgrath, S., Campbell, B., Lee, H., Herdy, J.R., et al. (2015). Directly reprogrammed human neurons retain aging-associated transcriptomic signatures and reveal age-related nucleocytoplasmic defects. Cell Stem Cell *17*, 705–718.

Miguel, L., Rovelet-Lecrux, A., Feyeux, M., Frebourg, T., Nassoy, P., Campion, D., and Lecourtois, M. (2019). Detection of all adult Tau isoforms in a 3D culture model of iPSC-derived neurons. Stem Cell Res *40*, 101541.

Miller, J.D., Ganat, Y.M., Kishinevsky, S., Bowman, R.L., Liu, B., Tu, E.Y., Mandal, P.K., Vera, E., Shim, J.W., Kriks, S., et al. (2013). Human iPSC-based modeling of late-onset disease via progerin-induced aging. Cell Stem Cell *13*, 691–705.

Mocanu, M.M., Nissen, A., Eckermann, K., Khlistunova, I., Biernat, J., Drexler, D., Petrova, O., Schönig, K., Bujard, H., Mandelkow, E., et al. (2008). The potential for beta-structure in the repeat domain of tau protein determines aggregation, synaptic decay, neuronal loss, and coassembly with endogenous Tau in inducible mouse models of tauopathy. J. Neurosci. *28*, 737–748.

Mungenast, A.E., Siegert, S., and Tsai, L.H. (2016). Modeling Alzheimer's disease with human induced pluripotent stem (iPS) cells. Mol. Cell Neurosci *73*, 13–31.

Nonaka, T., Watanabe, S.T., Iwatsubo, T., and Hasegawa, M. (2010). Seeded aggregation and toxicity of {alpha}-synuclein and tau: cellular models of neurodegenerative diseases. J. Biol. Chem. *285*, 34885–34898.

Pnevmatikakis, E.A., Soudry, D., Gao, Y., Machado, T.A., Merel, J., Pfau, D., Reardon, T., Mu, Y., Lacefield, C., Yang, W., et al. (2016). Simultaneous denoising, deconvolution, and demixing of calcium imaging data. Neuron *89*, 285–299.

Sanders, D.W., Kaufman, S.K., Devos, S.L., Sharma, A.M., Mirbaha, H., Li, A., Barker, S.J., Foley, A.C., Thorpe, J.R., Serpell, L.C., et al. (2014). Distinct tau prion strains propagate in cells and mice and define different tauopathies. Neuron *82*, 1271–1288.

Santacruz, K., Lewis, J., Spires, T., Paulson, J., Kotilinek, L., Ingelsson, M., Guimaraes, A., Deture, M., Ramsden, M., Mcgowan, E., et al. (2005). Tau suppression in a neurodegenerative mouse model improves memory function. Science *309*, 476–481.

Sentmanat, M.F., Peters, S.T., Florian, C.P., Connelly, J.P., and Pruett-Miller, S.M. (2018). A survey of validation strategies for CRISPR-cas9 editing. Scientific Rep. *8*, 888.

Shi, Y., Kirwan, P., Smith, J., Robinson, H.P., and Livesey, F.J. (2012). Human cerebral cortex development from pluripotent stem cells to functional excitatory synapses. Nat. Neurosci. *15*, 477–486, s1.

Spillantini, M.G., Crowther, R.A., Kamphorst, W., Heutink, P., and Van Swieten, J.C. (1998). Tau pathology in two Dutch families with mutations in the microtubule-binding region of tau. Am. J. Pathol. *153*, 1359–1363.

Sposito, T., Preza, E., Mahoney, C.J., Setó-Salvia, N., Ryan, N.S., Morris, H.R., Arber, C., Devine, M.J., Houlden, H., Warner, T.T., et al. (2015). Developmental regulation of tau splicing is

disrupted in stem cell-derived neurons from frontotemporal dementia patients with the 10 + 16 splice-site mutation in MAPT. Hum. Mol. Genet. *24*, 5260–5269.

Strang, K.H., Croft, C.L., Sorrentino, Z.A., Chakrabarty, P., Golde, T.E., and Giasson, B.I. (2018). Distinct differences in prion-like seeding and aggregation between Tau protein variants provide mechanistic insights into tauopathies. J. Biol. Chem. *293*, 2408–2421.

Tcw, J. (2019). Human iPSC application in Alzheimer's disease and Tau-related neurodegenerative diseases. Neurosci. Lett. *699*, 31–40.

Usenovic, M., Niroomand, S., Drolet, R.E., Yao, L., Gaspar, R.C., Hatcher, N.G., Schachter, J., Renger, J.J., and Parmentier-Batteur, S. (2015). Internalized tau oligomers cause neurodegeneration by inducing accumulation of pathogenic tau in human neurons derived from induced pluripotent stem cells. J. Neurosci. *35*, 14234.

Verheyen, A., Diels, A., Dijkmans, J., Oyelami, T., Meneghello, G., Mertens, L., Versweyveld, S., Borgers, M., Buist, A., Peeters, P., and CIK, M. (2015). Using human iPSC-derived neurons to model TAU aggregation. PLoS One *10*, e0146127.

Verheyen, A., Diels, A., Reumers, J., Van Hoorde, K., Van Den Wyngaert, I., Van Outryve D'ydewalle, C., De Bondt, A., Kuijlaars, J., De Muynck, L., De Hoogt, R., et al. (2018). Genetically Engineered iPSC-derived FTDP-17 MAPT neurons display mutation-specific neurodegenerative and neurodevelopmental phenotypes. Stem Cell Rep. *11*, 363–379.

Weaver, C.L., Espinoza, M., Kress, Y., and Davies, P. (2000). Conformational change as one of the earliest alterations of tau in Alzheimer's disease. Neurobiol. Aging *21*, 719–727.

Yu, X., Luo, Y., Dinkel, P., Zheng, J., Wei, G., Margittai, M., Nussinov, R., and Ma, B. (2012). Cross-seeding and conformational selection between three- and four-repeat human Tau proteins. J. Biol. Chem. *287*, 14950–14959.

Zhang, W., Falcon, B., Murzin, A.G., Fan, J., Crowther, R.A., Goedert, M., and Scheres, S.H.W. (2019). Heparin-induced tau filaments are polymorphic and differ from those in Alzheimer's and Pick's diseases. eLife *8*, e43584.

Zhang, W., Tarutani, A., Newell, K.L., Murzin, A.G., Matsubara, T., Falcon, B., Vidal, R., Garringer, H.J., Shi, Y., Ikeuchi, T., et al. (2020). Novel tau filament fold in corticobasal degeneration. Nature *580*, 283–287.

STAR★METHODS

KEY RESOURCES TABLE

REAGENT or RESOURCE	SOURCE	IDENTIFIER
Antibodies		
AP2α (Mouse monoclonal IgG1)	Developmental Studies Hybridoma Bank	Cat# 5E4, RRID:AB_2056333
AT8 (Tau pS202/pT205; Mouse monoclonal IgG1)	Thermo Fisher Scientific	Cat# MN1020, RRID:AB_223647
CP27 (total tau; Mouse monoclonal IgG2b)	P. Davies Albert Einstein College of Medicine; New York; USA	Cat# CP27, RRID:AB_2716722
CTIP2 (Rat monoclonal IgG2a; 25B6)	Abcam	Cat# ab18465, RRID:AB_2064130
FOXG1 (Rabbit polyclonal)	Abcam	Cat# ab18259, RRID:AB_732415
MAP2 (Chicken polyclonal IgY)	Abcam	Cat# ab5392, RRID:AB_2138153
MC1 (conformational tau; Mouse IgG1)	P. Davies Albert Einstein College of Medicine; New York; USA	Cat# MC1, RRID:AB_2314773
PAX6 (Rabbit polyclonal)	Biolegend	Cat# 901301, RRID:AB_2565003
PHF1 (Tau pSer396/pS404; Mouse monoclonal IgG1)	P. Davies Albert Einstein College of Medicine; New York; USA	Cat# PHF1, RRID:AB_2315150
RD3 (3R tau; Mouse monoclonal, 8E6/C11)	EMD Millipore	Cat# 05-803, RRID:AB_310013
SOX10 (Goat polyclonal)	R&D Systems	Cat# AF2864, RRID:AB_442208
SOX2 (Rabbit polyclonal)	Abcam	Cat# ab97959, RRID:AB_2341193
TauC (total tau; Rabbit polyclonal)	Agilent	Cat# A0024, RRID:AB_10013724
Tau phospho S422 (Rabbit monoclonal, EPR2866)	Abcam	Cat# ab79415, RRID:AB_1603345
TBR1 (Rabbit polyclonal)	Abcam	Cat# ab31940, RRID:AB_2200219
TUJ1 (Mouse monoclonal IgG2a)	Covance	Cat# MMS-435P, RRID:AB_2313773
Bacterial and virus strains		
AAV6-SYN1-GCaMP6f	Vigene Biosciences	N/A
Biological Samples		
Sarkosyl-insoluble AD brain material (SI-AD)	This paper	N/A
Sarkosyl-insoluble control brain material (SI-C)	This paper	N/A
MC1-immunopurified AD brain material (MC1-AD)	P. Davies Albert Einstein College of Medicine; New York; USA	N/A
Chemicals, peptides, and recombinant proteins		
LDN193189	Tocris	6053
SB431542	Tocris	1614
CHIR99021	R&D	4423
Cyclopamine	Millipore	239806
FGF2	R&D	233-FB-025
BDNF	Peprotech	450-02
GDNF	Peprotech	450-10
Dibutyryl cAMP	Peprotech	1698950
RO4929097	VWR	10192-018
DAPT	Tocris	2634
Laminin	Sigma	L2020

(*Continued on next page*)

Continued

REAGENT or RESOURCE	SOURCE	IDENTIFIER
Matrigel Growth Factor Reduced Basement Membrane Matrix ([protein] >9 mg/mL, endotoxin <1.5 EU/mL)	Corning	354230
Y-27632	Millipore	688000
Mitomycin C	Sigma	M4287
Recombinant 2N4R P301L rTau heparin-induced PHF	This paper	N/A
Recombinant 2N4R WT rTau heparin-induced PHF	This paper	N/A
Recombinant 2N3R WT rTau heparin-induced PHF	This paper	N/A
Critical commercial assays		
HTRF Tau Aggregation Kit	Cisbio	6FTAUPEG
V-PLEX Plus Aβ Peptide Panel 1 (4G8) Kit	Meso Scale Diagnostics	K15199G
V-PLEX Plus Human Total Tau Kit	Meso Scale Diagnostics	K151LAG
Experimental models: Cell lines		
IPSC0028	Sigma	IPSC0028
IPSC0028_MAPT-P301S/E10+16	Verheyen et al, 2018	N/A
IPSC0028_MAPT- E10+16	Verheyen et al, 2018	N/A
IPSC0028_MAPT-KO	This paper	N/A
IPSC0028_MAPT-WT (Untargeted)	This paper	N/A
IPSC0028_MAPT-P301S/E10+14/E10+16	This paper	N/A
IPSC0028_MAPT-E10+14	This paper	N/A
IPSC0028_MAPT-E10+14/E10+16	This paper	N/A
BIONi010-C-13	EBiSC	Cat# BIONi010-C-13, RRID:CVCL_RF90
Oligonucleotides		
Taqman assays, see Table S1	This paper	N/A
MAPT Knockout sgRNA: AACGAAGATCGCCACACCGC	This paper	WashU GEiC
MAPT Knockout target region amplification: Fwd gcggagtggggctggtgttgactct, Rev ctgaccagctgccaggggttattca	This paper	WashU GEiC
MAPT 10+14, 10+16 mutation sgRNA: ACGGCGCATGGGACGTGTGA	This paper	WashU GEiC
MAPT 10+14 mutation donor: aagtgtacgcactcacaccacttcctaataatt caagccacagcacggcgcatgggacGtAtg aaggtactcacactgccgcctcccgggacgtg tttgatattatcctttgagccacact	This paper	WashU GEiC
MAPT 10+14, 10+16 mutation donor: gcaagtgtacgcactcacacca cttcctaataattcaagccacagcacggcg catgggacAtAtgaaggtactcacactg ccgcctcccgggacgtgtttgatattatcc tttgagccacact	This paper	WashU GEiC

(*Continued on next page*)

Continued

REAGENT or RESOURCE	SOURCE	IDENTIFIER
MAPT 10+14, 10+16 mutation target region amplification primers: Fwd cccagactgcctctgccaagtccga, Rev: gggagccgggctacattcacccaga	This paper	WashU GEiC
Software and algorithms		
Harmony High-Content Imaging and Analysis Software	Perkin Elmer	HH17000010
GenEx Professional Software Package, Version 6	MultiD Analyses AB	N/A
Other		
Phalloidin-AlexaFluor568	Thermo Fisher Scientific	A12380

RESOURCE AVAILABILITY

Lead contact

Further information and requests for resources and reagents should be directed to and will be fulfilled by the Lead Contact, Justine Manos (justine.manos@abbvie.com).

Materials availability

Due to contractual obligations, Abbvie is not permitted to share the human iPSC lines that were generated in this study. However, parental hiPSC lines used in this study are commercially available and detailed information has been provided in the methods section to establish the specified gene edits, which were performed by a contract research organization.

Data and code availability

- All data reported in this paper will be shared by the lead contact upon request.
- This paper does not report original code.
- Any additional information required to reanalyze the data reported in this paper is available from the lead contact upon request.

EXPERIMENTAL MODEL AND SUBJECT DETAILS

Human iPSC lines, culture, and MAPT editing

Daughter lines derived from the commercially available female hiPSC line IPSC0028 (Sigma-Aldrich) were used for the majority of experiments, except where indicated. Characterization of the hiPSC lines confirming expression of pluripotency markers, a normal karyotype, and differentiation into all three germ layers was performed by the manufacturer. Gene editing to introduce the E10 + 16 and/or P301S mutations were performed previously by Sigma using zinc finger nuclease technology (Verheyen et al, 2018). Additional gene editing presented here was performed at the Genome Engineering and iPSC Center at Washington University School of Medicine. Using CRISPR/Cas9 ribonucleoproteins with IVT sgRNA, knockout editing was achieved by targeting exon 1 while exon 10 editing was achieved by targeting the 5′ splice site. To utilize the most appropriate isogenic control when working with gene edited lines, *MAPT*-WT untargeted hiPSC-neurons were derived from a subclone of the parent hiPSC line that went through the CRISPR/Cas9 knockout editing process but was not successfully edited. All data related to *MAPT*-WT cells presented in this manuscript use this untargeted cell line and not the parental line. Targeted-deep sequencing was used to validate reagents and confirm single cell derived clone genotypes as previously described (Chen and Pruett-Miller, 2018; Sentmanat et al, 2018). See key resources table for relevant sequences. All hiPSCs were deemed pluripotent using Pluritest (ThermoFisher) and karyotypically normal by KaryoStat (ThermoFisher) and/or G-banding (Washington University GEiC) (*data not shown*). Gene editing outcomes were confirmed in hiPSC-neurons by qPCR and Western blot analysis. Human iPSCs were maintained on Matrigel Growth Factor Reduced Basement Membrane Matrix (<1.5 EU endotoxin; >9 mg/mL; Corning)

in StemFlex Complete Medium (ThermoFisher) at 37°C and 5% CO_2. Human iPSCs were maintained via clump-passaging using ReLeSR (StemCell Technologies). Prior to use, frozen Matrigel aliquots were thawed overnight at 4°C in a Styrofoam rack, diluted to 77.5 μg/mL in DMEM/F12 + HEPES (ThermoFisher). Tissue culture treated flasks/plates were immediately coated and stored for a minimum of 16 h at 4°C.

Brain tissue

Frozen human frontal cortical brain tissue from AD (Braak stage V/VI) and non-AD (Braak stage 0/I) male and female donors used in preparing sarkosyl-insoluble tau seeds were generously provided by the Massachusetts Alzheimer's Disease Research Center or purchased from Folio (now Discovery Life Sciences). As the level of tau pathology varies between regions of the frontal cortex, we first divided large (usually >10 g/piece) frozen tissues into smaller pieces (0.5–1 mg/piece) for randomization, then prepared aliquots of large stocks of lysates made from multiple pieces of tissue for future use. Tau pathology of these tissues was confirmed using Western blot analysis of pathological tau species, Importantly, lysates derived from AD brains that have low levels of tau aggregates were excluded from further use (*data not shown*). MC1-immunopurified AD brain material (MC1-AD) was kindly provided by Peter Davies.

METHOD DETAILS

hiPSC differentiation to cortical neurons

Pluripotent hiPSCs were differentiated into forebrain neural progenitors and cortical neurons according to a modified published protocol (Cao et al, 2017; Chambers et al, 2009; Gaspard et al, 2008; Hansen et al, 2011). Briefly, differentiation was initiated using hiPSC cultures containing large, homogeneous colonies with phase bright borders and <5% spontaneous differentiation present. Cells were harvested with Accutase (ThermoFisher) and plated at 500,000 cells per cm^2 onto 77.5 μg/mL Matrigel-coated 6-well plates in StemFlex Complete supplemented with the ROCK1 inhibitor RevitaCell (ThermoFisher). The next day ("Day 0"), confluent hiPSCs were switched to Essential 6 medium (ThermoFisher) supplemented with 500 nM LDN193189 (StemGent), 10 μM SB431542 (R&D Systems), and 500 nM CHIR99021 (R&D Systems). On Day 2, CHIR99021 was replaced by 5 μM Cyclopamine (Millipore). Essential 6 was gradually exchanged with N2B27 medium (Advanced DMEM/F12, Neurobasal medium, N2 supplement, B27 supplement without vitamin A, pen/strep, GlutaMax; ThermoFisher). Starting Day 3, Laminin (Sigma) was added at 1 μg/mL concentration to help prevent cell lifting. Nine days after initiation, the cells were harvested with Accutase and plated at 1.5 million cells per cm^2 in N2B27 medium supplemented with 10 μM Y-27632 (Millipore). In cases with evidence of high neural crest contamination (indicates high Wnt signaling at pluripotent stage), differentiation was repeated without CHIR99021. 10 ng/mL FGF2 (Millipore) was briefly added to the medium until Day 15 when neural rosettes are observed. On Day 17, hiPSC-NPCs were collected with Accutase, resuspended in N2B27 medium +10% DMSO at 10 million cells per mL, and frozen overnight at −80°C in a controlled vessel at 1°C per minute before being transferred to LN_2 vapor for long-term storage. Synchronization of hiPSC-NPC differentiation to neurons is achieved by thawing frozen vials (considered "DIV -8") onto 77.5 μg/mL Matrigel-coated plates at 350,000 cells per cm^2 in N2B27 medium supplemented with 10 μM Y-27632 (Millipore) and subsequent culturing with N2B27 medium supplemented with 500 nM LDN193189 and 5 μM Cyclopamine. Neuronal differentiation is encouraged with the addition of the γ-secretase inhibitor RO4929097 (VWR) at 500 nM on DIV -5. For final neuron replating, black 96-well plates (Corning/Fisher 353,219 or PerkinElmer Cell Carrier Ultra) are treated with 0.01% Poly-L-ornithine (PLO; Sigma) solution overnight at room temperature. The next day, PLO is completely aspirated and plates are then coated with 28 μg/mL Matrigel diluted in DMEM/F12 + HEPES and stored at 4°C overnight. On DIV 0, cells are harvested with Accutase, passed through a 40 μm cell strainer (VWR) to remove residual cell clusters, centrifuged at 300 xg for 5 min, and plated onto PLO-treated/Matrigel-coated plates at ~110,000 cells per cm^2 (35,000 cells per 96-well) in NB27 + medium (Neurobasal Plus medium, B27 Plus supplement, pen/strep, GlutaMax; ThermoFisher) supplemented with 10 μM Y-27632, 500 nM RO4929097, 10 ng/mL BDNF, 200 μM Ascorbic Acid, 250 μM dcAMP, 5 ng/mL GDNF, and 1 μg/mL Laminin. Greiner μClear and other Corning microwell plates, poly-D-lysine plus laminin or Matrigel-only coating, and cell densities <75,000/cm^2 or >145,000/cm^2 resulted in neuronal death or clumping. On DIV 2, hiPSC-neurons are optionally treated with 0.5 μg/mL Mitomycin-C (Sigma) diluted in Neuronal Maintenance Medium (NMM; NB27 + supplemented with 10 ng/mL BDNF, 200 μM Ascorbic Acid, 250 μM dcAMP, 5 ng/mL GDNF, and 1 μg/mL Laminin) for 1 h in the incubator (37°C with 5% CO_2). After incubation, two-thirds of the well volume is removed and replaced with fresh NMM supplemented with 500 nM RO4929097. The hiPSC-neurons are maintained with half volume media changes twice weekly with fresh NMM. Basic cell health (neurite outgrowth, absence of neuron clustering or overt cell death)

are monitored using the EVOS microscope (ThermoFisher). For generation of neurons from the BIONi010-C-13 hiPSC with doxycycline – inducible overexpression of iNGN2, cells were seeded with 10 μM Y-27632 at 25,000 cells per cm^2 one day prior to the induction on Matrigel-coated plates. Neural induction was initiated by exchanging the medium against N2B27 medium supplemented with 2 μg/mL doxycycline (Sigma-Aldrich) for two days with daily medium changes. Cells were replated after two days of induction in NMM medium on PLO/Matrigel-coated plates, as described above. Medium was additionally supplemented with 2 μg/mL doxycycline, 10 μM Y-27632, 500 nM RO4929097 for one day, until it was exchanged against the same medium without Y-27632. Further medium changes were performed with half-volume medium changes with NMM, as indicated above.

Cell characterization immunofluorescence

hiPSCs and hiPSC-NPCs were fixed using 4% paraformaldehyde (PFA) and incubated at room temperature for fifteen minutes. hiPSC-neurons were fixed with 4% PFA added to cell culture medium at 50% for twenty-five minutes to maintain neuron attachment. After fixation, cells were washed with PBS, wrapped in parafilm and stored at 4°C prior to staining. PFA-fixed hiPSCs and hiPSC-derived cells were treated with blocking/permeabilizing buffer consisting of 3% BSA +0.3% Triton X-100 in PBS for 25 min (45 min for hiPSC-neurons) at room temperature. Primary antibodies were diluted in blocking/permeabilizing buffer and incubated on cells overnight at 4°C. After several washes with PBS, AlexaFluor secondary antibodies (ThermoFisher) were diluted at 1:500 in blocking/permeabilizing buffer and incubated for one hour at room temperature while protected from light. After several washes with PBS, DAPI was diluted in PBS and incubated for seven minutes at room temperature while protected from light. After incubation, cells were washed with PBS, protected from light, and stored at 4°C. To remove debris and improve imaging, all primary and secondary antibody dilutions and DAPI were filtered through a Spin-X column (VWR 29442-752) before being added to the cells.

Analysis of secreted Aβ

At the time of replating (DIV0), hiPSC-neurons were treated with either DMSO, 10 μM DAPT, or 500 nM RO4929097. Two weeks later, the media was completely replaced with fresh neuronal maintenance medium, and some wells were re-treated with 400 nM DAPT to assess whether the hiPSC-neurons were still responsive to GSI treatment. Forty-eight hours later, media was collected from 1 well of a 24-well plate per sample and spun at 1200 xg for 10 min at 4°C to remove debris. The supernatant was transferred to a fresh tube and snap frozen prior to analysis. Media samples were then thawed on ice, and Aβ40 and Aβ42 were measured using the V-PLEX Plus Aβ Peptide Panel 1 (4G8) Kit from Meso Scale Diagnostics according to the manufacturer's instructions. Values were normalized to the cell number based on the DAPI quantification from parallel wells to account for the NPC proliferation in wells not treated with DAPT or RO4929097.

Calcium imaging

AAV6-syn-GCaMP6f purchased from Vigene Biosciences was diluted with NMM and applied to the differentiated hiPSC-neurons of DIV 7 to achieve 25k MOI (multiplicity of infection). After 7 days of expression, longitudinal calcium imaging was performed by a high-content imaging machine (PerkinElmer Opera Phenix). For each imaging, 1000 frames of images were continuously acquired at 3 Hz. During imaging, temperature and CO_2 were maintained at 37 C and 5%, respectively. The raw images were processed by a constrained nonnegative matrix factorization (CNMF) algorithm (Pnevmatikakis et al, 2016) to determine whether individual neurons were fired at given time point. Then, circuit maturation of the hiPSC neurons in tau aggregation assay time window was evaluated by quantifying group firing events of neurons.

Brain-derived tau seeds

Preparation. MC1-immunopurified brain (MC1-AD) seeds generously provided by Peter Davies were sonicated using the QSonica Sonicator (20 s cycle, with 2 s ON and 1 s OFF, 20% amplitude), aliquoted, and stored at −80°C. For sarkosyl-insoluble seeds (SI-AD and SI-C), brain tissue from pathology-confirmed AD or non-AD donors purchased from Folio brain bank was homogenized in 5μL/mg TBS lysate buffer using the Presellys Evolution (CKMix, 2 mL tube, 5500 speed, 1 cycle, 20 s, pause 120 s, 2 rounds). Sarkosyl extraction was performed according to Guo et al. (Guo and Lee, 2011). Briefly, brain lysates were centrifuged at 27, 000 x g for 20 min at 4°C in two successive rounds. The supernatants were pooled and incubated with 1% sarkosyl solution for 1.5 h (h). Samples were then centrifuged at 250,000 x g for 1.5 h at

4°C. The pellet was resuspended in TBS buffer, sonicated for 30 s (qSonica Q125 model), and centrifuged at 100,000 x g for 1 h at 4°C. The pellet was resuspended in sterile PBS and centrifuged at 100,000 x g for 30 min at 4°C, and the supernatant was used for seeding experiments. Enriched SI-AD and SI-C were characterized by MSD and Western blot to confirm tau pathology prior to use (*data not shown*).

Tau measurement. Total tau levels were measured using the V-PLEX Human Total Tau Kit from Meso Scale Discovery. Sarkosyl insoluble fractions and MC1-antibody purified PHFs were diluted to a 5x working stock with 4x Laemmlli buffer and β-mercaptoethanol. Samples were boiled at 95°C for 5 min and further diluted with Diluent 35 to a final dilution of 5000x. For the standard curve, the tau calibrator was prepared at 28,800 pg/mL and serially diluted 3-fold. The plates were blocked using diluent 35 for one hour at room temperature followed by three washes with 0.05% PBST. The samples were added along with the calibrator and incubated on a shaker for 1 h at room temperature. Plates were washed with 0.05% PBST, and the SULFO-TAG Anti-Total Tau antibody (diluted from 50x to 1x with diluent 35) was added to the plates and incubated for one hour at room temperature on a shaker. The read buffer (diluted from 4x to 1x) was added to the plates, and after 8 min the plates were read using the Sector® Imager 6000.

Characterization – Normal and AD human brain tissue samples (Folio) were weighed and lysed in supplemented PBS at 5μL/mg of tissue. Tissues were homogenized on the Precellys tissue homogenizer (6600rpm, 2 × 20s for 120 s) and the homogenate was collected in 15mL falcon tubes. Homogenates were spun for 5 min at 3000xg at 4°C, supernatant was collected and characterized using various biochemical and cellular assays. Brain lysates were prepared for Western blot analysis using LDS sample buffer (ThermoFisher Scientific, MA) and reducing agent containing DTT (Thermofisher Scientific, MA). Samples were boiled at 95°C for 5 min on a heating block and the heat-treated samples were separated by gel electrophoresis on a 4-12% NuPAGE Bis-Tris gel (Thermofisher Scientific, MA). Precision-plus dual color protein standard was used as the ladder (Biorad Laboratories, CA). After the electrophoresis run, the gel was transferred using the iBlot2 dry blotting system (Thermofisher Scientific, MA) on to a pre-activated PVDF membrane using the P0 program. The membranes were then blocked using the Intercept® blocking buffer (LI-COR Biosciences, NE) for 1 h at RT on a shaker. Polyclonal rabbit total tau TauC (Agilent Technologies, CA) and mouse monoclonal PHF1 antibodies were added to the membranes and incubated overnight on a shaker at 4°C. The following day, the membranes were washed with 1 × 0.05% TBST and incubated with Licor IRDye™ anti-mouse (680RD) and anti-rabbit (800CW) secondary antibodies (LI-COR Biosciences, NE) at 1:5000 for 1 h at RT. The membranes were then washed with 1x TBST and then imaged on the Licor Odyssey CLX system (LI-COR Biosciences, NE).

Recombinant tau seeds

Recombinant tau PHFs were prepared by heating 40 μM human tau monomer in PBS supplemented with 2 mM DTT to 50°C for 15 min and then cooled down to 37°C. Heparin was added to a final concentration of 40 μM, and the mixture was shaken for 6-7 days (550 rpm) at 37°C. 1 mM DTT was added daily to reduce disulfide bonds. PHFs were centrifuged for 3 h at maximum speed in a tabletop centrifuge at 4°C to pellet the PHFs. The supernatant (containing buffer with DTT) was removed, and the pellet was resolved in an equal volume of PBS without DTT to remove DTT and any remaining aggregation-incompetent tau material from the seed preparation. The PHFs were sonicated for 30 min (50% amplitude, short intervals of sonification on ice), and the concentration was confirmed using a BCA assay according to the manufacturer's instructions. Sonicated PHFs were aliquoted in low-binding Eppendorf tubes and stored at −80°C until later use. 40 μM aliquots were thawed on ice and diluted to 800 nM in ice-cold 1X PBS in (Costar) 1.5 mL low-binding microcentrifuge tubes. The tube opening was covered with parafilm, a small hole was created, and the 800 nM diluted aliquots were sonicated using the QSonica Sonicator (20 s cycle, with 2sec ON and 1sec OFF, 20% amplitude) on ice 3 times, while mixing tube contents in between each sonication. After sonication, 100 μL aliquots were prepared, snap-frozen on dry ice, and stored at −80°C for experimental use. The *in vitro* aggregation assay was performed in small volumes of 25 μL in a 384well plate (Greiner). Recombinant hTau (2N4R P301L) was diluted to a concentration of 40 μM in PBS and heated to 50°C for 15 min with 2mM DTT. 40 μM of Heparin, 1 mM DTT and 20 μM Thioflavin T were added to the reaction. The Thioflavin T fluorescence was measured every 30 min for a total of 72 h with the Cytation5 plate reader function (excitation: 440 nm, emission: 480 nm). The plate was thereby incubated at 37°C with continuous shaking. For transmission electron miscroscopy, glow-discharged 400 mesh cu/pd grids coated with formvar and a 4 nm carbon layer were used. Samples at a concentration of around 40μM Tau were diluted 1:100 in ddH20 and added to the grid for 1 min. The grid was washed with ddH20 and stained with 2% uranyl

acetate for 1 min, blotted and left to dry. Images were acquired using a Biotwin CM120 Philips electron microscope with a laB6 cathode at 100 kV.

Tau aggregation assay

After the final replating, hiPSC-neurons were matured for 16 days (except where indicated) before adding tau seeds. Tau seed aliquots were thawed on ice prior to use. Tau seeds were diluted in fresh NMM. Two-thirds of the well volume (100 μL) was removed and replaced with 50 μL fresh NMM + tau seeds. Three days later, one-half of the well volume was removed (50 μL) and replaced with fresh NMM (100 μL). hiPSC-neurons were fed twice weekly with 50% fresh NMM media changes and cultured at least four weeks until methanol fixation.

Tau aggregation immunofluorescence

For analysis of insoluble tau aggregates, hiPSC-neurons were fixed with 100% ice-cold methanol for fifteen minutes at −20°C. After fixation, cells were washed with PBS, wrapped in parafilm and stored at 4°C prior to staining. Fixed cells were treated with blocking buffer consisting of 3% BSA in PBS for 45 min at room temperature. Primary antibodies were diluted in blocking buffer before being added to the cells used and incubated overnight at 4°C. After several washes with PBS, AlexaFluor secondary antibodies (ThermoFisher) were diluted at 1:500 in blocking buffer and incubated for one hour at room temperature while protected from light. After several washes with PBS, DAPI was diluted in PBS and incubated for seven minutes at room temperature while protected from light. After incubation, cells were washed with PBS, protected from light, and stored at 4°C. To remove debris and improve imaging, all primary and secondary antibody dilutions and DAPI were filtered through a Spin-X column (VWR 29442-752) before being added to the cells.

Fluorescence microscopy

High content immunofluorescence imaging was conducted on either the Operetta or Opera Phenix instrument (PerkinElmer) using Harmony (PerkinElmer) for image acquisition and analysis. Immunofluorescence-stained plates were brought to room temperature before imaging to prevent image-capture errors due to condensation. For cell characterization, imaging was performed using a 20X water objective and confocal settings with a 10-layer z-stack (1 μm increments). For tau aggregation, imaging was performed using a 40X water objective and confocal settings with a 7-layer z-stack (1 μm increments). All fluorescence images are displayed as maximum projections of the collapsed z-stack. For evaluating intracellular localization of tau seeds, laser scanning confocal microscopy was performed using the Zeiss LSM880. 10 layer z-stack images with 1 μm increments were acquired with 63x oil objective (NA 1.4) and colocalization of tau seeds (MC1) and the somatodendritic marker (MAP2) was evaluated by Zen Blue (Zeiss).

Western blot analysis

Preparation of dephosphorylated cell lysates. Human iPSC-neurons matured for 21-28 or 126 days were rinsed with ice-cold PBS and scraped using a cell lifter (Costar). Cell suspensions were collected into microcentrifuge tubes and spun for 10 min at 10,000 xg at 4°C. Cell pellets were lysed in RIPA buffer (Sigma, MO) supplemented with cOmplete™ protease inhibitors (Millipore Sigma, MA) and sonicated at 20% amplitude, 2sec on, 1 sec off for 20 s on ice on the Q125 (QSonica LLC, CT). Sonicated lysates were then spun down for 30 min at 3000xg at 4°C and the supernatant was collected for total protein analysis using the micro-BCA assay (ThermoFisher, MA). After normalizing all the cell lysates to the same total protein concentration, 30μL of each sample was added to 10μL of lambda phosphatase enzyme mix (New England Biolabs, MA) and incubated for 3 h at 30°C in a water bath. Dephosphorylated cell lysates were prepared for Western blot analysis using LDS sample buffer (ThermoFisher) and reducing agent containing DTT (ThermoFisher).

Preparation of sarkosyl soluble/insoluble cell lysates. Approximately 1 million seeded hiPSC-neurons (4 weeks post-seeding) in a 6-well were lysed in 100 μL RIPA buffer (Sigma, MO) supplemented with protease and phosphatase inhibitors (Millipore Sigma) for 5 min at room temperature. Following collection, the lysed samples were incubated on ice for an additional 5 min before spinning for 1 min at 14,000 rpm at 4°C. The supernatant was transferred to a fresh microcentrifuge tube, snap frozen on dry ice, and stored at −80°C until the sarkosyl extraction. At the time of extraction, samples were thawed on ice and 80 μL was transferred to a fresh microcentrifuge tube and sarkosyl (Sigma, MO) was added to a final

concentration of 1%. Samples were incubated for 30 min at room temperature on an inverting rotor then transferred to ultracentrifuge tubes. Samples were spun at 150,000 xg for 30 min at 4°C in an Optima MAX XP ultracentrifuge (Beckman Coulter). The supernatant representing the soluble fraction was transferred to a fresh microcentrifuge tube, and the pellet was resuspended in 80 μL RIPA buffer containing protease and phosphatase inhibitors and 1% sarkosyl. Samples were spun again at 150,000 xg for 30 min at 4°C, and the pellet representing the insoluble fraction was resuspended in 15 μL 1x NuPage LDS sample buffer plus reducing agent (ThermoFisher Scientific). 5μL of soluble fraction was diluted with 2x sample buffer and run in parallel.

Blotting. Cell lysates were boiled at 95°C for 5 min on a heat block and then separated by gel electrophoresis on a 4-12% NuPAGE Bis-Tris gel (ThermoFisher). A recombinant tau ladder (EMD Millipore, MA) was used as a positive control for the detection of the different tau isoforms. Subsequently, the gel was transferred using the iBlot2 dry blotting system (Thermofisher Scientific, MA) onto a pre-activated PVDF membrane using the P0 program. The membranes were then blocked using the Intercept® blocking buffer (LI-COR Biosciences, NE) for 1 h at RT on a shaker and stained with TauC (Agilent Technologies, CA), a polyclonal rabbit total tau antibody, and RD3 (EMD Millipore, MA), a 3R-specific antibody, at 1:3000 and 1:200, respectively. The membranes were incubated with the primary antibody overnight on a shaker and 4°C. The membranes were washed with 1 × 0.05% TBST and then incubated with Licor IRDye™ anti-mouse (680RD) and anti-rabbit (800CW) secondary antibodies (LI-COR Biosciences, NE) at 1:5000 for 1 h at RT. The membranes were then washed with 1x TBST and imaged on the Licor Odyssey CLX system (LI-COR Biosciences, NE). To calculate 4R:3R ratios, quantification of the bands was performed using the Licor imaging software.

HTRF

The Homogenous Time Resolved Fluorescence (HTRF; Degorce et al, 2009) Tau aggregation kit (Cisbio, MA) was used to determine tau aggregate levels in hiPSC neuron lysates using Fluorescence Resonance Energy Transfer (FRET). Cells were scraped in ice-cold PBS and pelleted followed by lysis in M-PER buffer. Serially diluted cell lysates, AD or control brain tissue, SI-AD seeds and 2N4R P301L sPHF seeds were tested in duplicate in a 384 well plate (Greiner Bio-one, Austria). Anti Tau-d2 and anti tau-Tb conjugates were diluted 1:50 from stock to a final volume, which was calculated based on the total number of samples. The two conjugates were diluted separately, mixed at equal ratios and vortexed before being added to the protein lysates on the plate at 10μL per well. Lysates and conjugates were then incubated overnight for 16 h and the plate was read on the Biotek SynergyH1 (Agilent Technologies, CA) using the HTRF filter cube which allows for sequential detection of Donor and Acceptor fluorescence. Results were plotted as the peak ratio of 655nM (acceptor fluorescence) to 620nM (donor fluorescence).

RNA isolation and quantitative PCR

Total RNA was prepared from hiPSC cultures using the MagMAX™ mirVana™ Total RNA Isolation Kit (ThermoFisher Scientific) according to the manufacturer's instructions. The integrity (RIN score) and concentration of the RNA was determined using an Agilent Tapestation. RIN scores ranged from 9 to 10. RNA concentrations were adjusted to 20 ng/ul and reverse transcription was performed with Superscript IV VILO (ThermoFisher Scientific) in a 20ul reaction with 320ng per sample. The cDNA yield for each reaction was determined using Quant-iT™ OliGreen® reagent (ThermoFisher Scientific) and the cDNA concentrations were normalized to 5 ng/ul. Samples were subjected to qPCR analysis using the Juno/Biomark HD high throughput platform (Fluidigm). Briefly, cDNA was preamplified for 15 PCR cycles in a multiplex fashion using a panel of 96 Taqman assays (ThermoFisher Scientific, see Table S1). Following 10-fold dilution with water, the preamplified samples were prepared for loading onto the integrated fluidic circuit in accordance with the manufacturer's protocol. Data analysis was performed using the GenEx Professional software package, version 6 (MultiD Analyses AB). Starting with the raw Ct values, the Normfinder feature of the software was used to identify the most robust normalization scheme, resulting in the use of the 12 most stable transcripts to convert raw Cts into delta Ct values (referred to as global normalization). Next, after designating specific samples as the reference group, differential expression was calculated using the 2^-(delta Ct) method. Principal component analysis (PCA) was done using the default parameters in the GenEx package after importing the log2 values from the differential expression analysis. The heatmap was generated using Morpheus (https://software.broadinstitute.org/morpheus) using 2^-(delta Ct) values based on global normalization of the data.

QUANTIFICATION AND STATISTICAL ANALYSIS

For day 10 characterization, nuclear staining for Pax6, Sox10, and AP2α was quantified by first defining the DAPI + nuclear area followed by the fluorescence intensity of the marker of interest. Fluorescence intensity thresholds were set based on non-overlapping signals for the three markers to define positive and negative cells. For aggregation analyses, tau aggregates were defined using MC1 staining and the Find Spot algorithm. Fluorescence intensity thresholds were set based on positive and negative controls on the same plate, and spots with a pixel area less than 7 were excluded. MAP2 area was quantified using the sum of the area defined by Image Region. All data analysis was performed using GraphPad Prism Software. Statistical analysis comparing multiple groups was performed using a one-way ANOVA with a Dunnett's multiple comparison test (3 groups) or with a Tukey's multiple comparison test (>3 groups) or a two-way ANOVA with a Tukey's multiple comparison test as indicated in the figure legends. Data are depicted with bar graphs as the mean +SD. Significance was defined as $p < 0.05$ (****$p < 0.0001$, ***$p < 0.001$, **$p < 0.01$, *$p < 0.05$). n indicates independent measures from individual wells. Independent experiments are displayed as separate graphs.